Journal of Electronics and Electrical Engineering
https://ojs.wiserpub.com/index.php/JEEE

Research Article

Design, Dynamic Modelling, Simulation and Control of a Solar Powered Sucker Rod Oil Pump

Charles Aimiuwu Osaretin[1*], Mohammad Tariq Iqbal[1], Stephen Butt[2]

[1] Department of Electrical and Computer Engineering, Memorial University of Newfoundland, St. John's, NL, Canada
[2] Department of Earth Sciences, Memorial University of Newfoundland, St. John's, NL, Canada
E-mail: caosaretin@mun.ca

Received: 30 November 2024; **Revised:** 1 January 2025; **Accepted:** 14 January 2025

Abstract: The sucker rod pump is a crucial artificial lift system widely deployed in the oil industry to extract crude oil from producing wells. Accurate modelling of the sucker rod pump has become essential as a viable strategy for optimizing performance, and ensuring both efficient and economic operation. This paper presents a comprehensive methodology for the design, dynamic modelling, simulation, and control of a solar-powered sucker rod oil pump. It combines load modelling of the sucker rod pump using SolidWorks with design, dynamic modelling, simulation, and control of the solar microgrid in Matlab's Simscape and Simulink. The model seamlessly integrates the mechanical and electrical systems with 100% renewable energy to power the sucker rod pump system. This approach combines the solar photovoltaic system, battery charge control system, battery energy storage system, step-up transformer, and the squirrel cage induction motor, which serves as the electric motor prime mover. The surface pump model is first developed in SolidWorks and then converted to Simscape, the rating of the pump is then implemented as a load in the solar-powered electrical microgrid. Environmental conditions such as solar irradiance and ambient temperature for summer and winter are obtained from data repositories and included in the modelling and analysis of the overall system performance demonstrating stable operation, robustness, and resilience to changing environmental and operational conditions.

Keywords: solar, sucker rod pump, dynamic modelling, renewable energy

1. Introduction

As global energy demand continues to increase, the oil and gas industry ironically continues to suspend, orphan, and abandon oil wells at an alarming rate due to technical, policy, and environmental reasons [1]. The increasing demand to reduce the energy footprint of producing wells is compounded by the leakage of methane and other potent greenhouse gases from idle and inactive wells [2]. Electricity cost constitutes a significant part of the overheads incurred in producing wells and with these wells sufficiently remote from the electric grid, onsite generation of 100% renewable energy presents a promising opportunity to invest in solar and wind energy microgrids, providing the energy required to restore these inactive oil wells to production while investing in distributed generation from 100% renewable energy powered microgrids [3]. This ensures that the landowners continue to earn lease revenue, and well operators remain in business, sustaining the income for site operators, tax revenue for the government, and employment for engineers when production from these legacy wells is sustainably restored. It also reduces the carbon footprint of these idle wells, as restoring them to production

DOI: https://doi.org/10.37256/jeee.4120256168

curtails the unintended emissions from the well [4]. Over 50% of all oil wells worldwide have an artificial lift system installed. Approximately 40% use the sucker rod pump as shown in Figure 1. It accounts for approximately 500,000 beam pumps worldwide [5], hence the selection of sucker rod pump (SRP) artificial lift technology for this study given its widespread use in the oil industry.

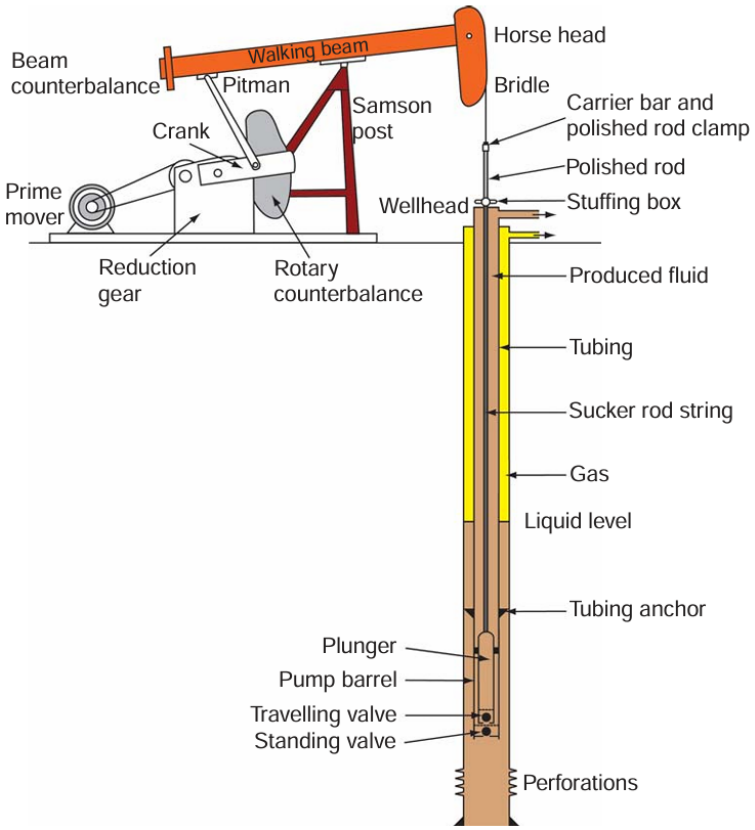

Figure 1. The sucker rod pumping system [6]

The Canadian province of Alberta has historically been one of the largest oil producers in Canada. Still, the province's upstream oil and gas sector reportedly contributed substantial methane emissions, accounting for approximately 70% of Alberta's emissions in 2014 [7]. The scale of Alberta's petroleum industry is evident in its vast number of registered wells, which exceeds 470,000 in 2024 [8]. Among these, a considerable number—around 155,000—are currently inactive, awaiting either reactivation or permanent decommissioning and land reclamation. More specifically, the Petrinex Alberta Public Data database indicates that about 81,000 wells in the province are classified as suspended [9]. The surface location of inactive petroleum wells in Alberta, Canada is given in Figure 2.

The cost of orphaned well clean-up in Canada is estimated to reach $1.1 billion by 2025 [10], hence with the growing energy demand and the regulatory requirement to reduce the carbon intensity of the Canadian upstream oil and gas sector, the adoption of renewable energy is gaining attention to reduce the impact of oil production on the electrical grid and mitigate the associated cost of electricity required to pump the ageing wells [11, 12]. The feasibility of combining PV with diesel for powering oil wells is considered in [13]. In previous research by the author, the technical and economic feasibility of using 100% renewable energy in powering inactive wells was examined [14]. The goal of this study is to model a sucker rod pump as a load and incorporate its rating in designing, modelling, and controlling a 100% solar-powered microgrid. The electric motor prime mover in Simscape is driven by a 100% solar-powered microgrid consisting of solar PV arrays, a charge controller, battery storage, a 3-phase inverter, a transformer, and a 3-phase squirrel cage induction motor.

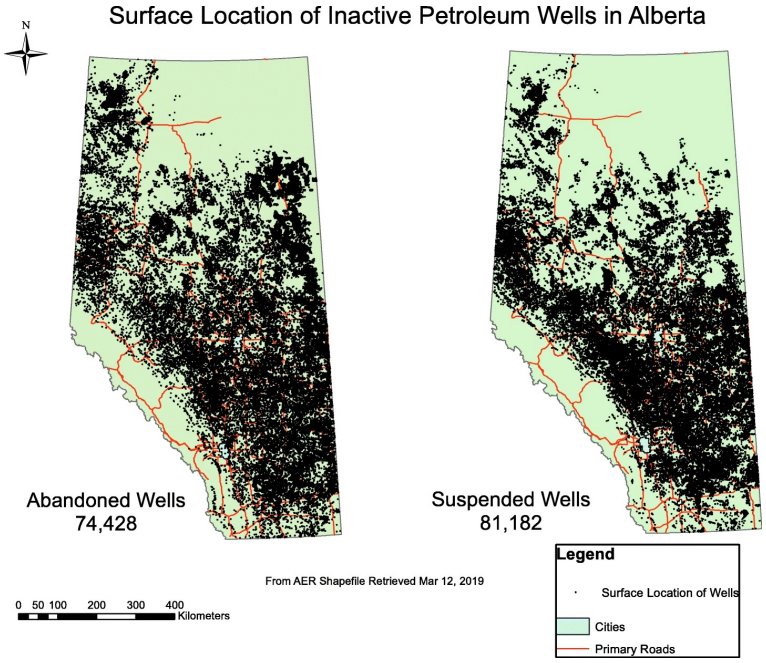

Figure 2. Surface location of inactive petroleum wells in Alberta, Canada [9]

2. Objectives

The objective of this paper is to develop a model-based simulation of the solar-powered sucker rod pump's behavior, allowing for the identification of opportunities for efficiency optimization at each subsystem. The study decouples the microgrid into subsystems, supporting efficiency enhancements and performance improvement across the entire system from solar PV source to electric motor load. The work supports adaptation to various environmental and operating conditions, so the system behavior can be analyzed and potential issues identified and addressed before prototyping and real-world implementation. The study incorporates load modelling from SolidWorks and Simscape into the Simulink model, providing a realistic representation of the actual system, and leading to more representative simulation results. The robust approach combines mechanical (SolidWorks) and electrical (Simscape) models which are crucial for designing effective controls for the sucker rod pump. The study begins with load modelling of the sucker rod pump system, utilizing SolidWorks for geometry development and translating to a Simscape model in capturing the functional mechanical and electrical characteristics of the pump. This is followed by the Solar PV array source design and modelling, including panel configurations, charge controller, power inverter, and step-up transformer for conditioning the inverter output to the load requirements. Energy storage system modelling incorporates a battery storage model to address the intermittent nature of solar power and ensure consistent and reliable operation of the oil pump. The control system for the system is designed and implemented to optimize power flow, manage battery state of charge (SOC), and ensure efficient pump operation. Extensive simulations under various environmental conditions are performed to evaluate system behavior and stability. The design is iterated to improve overall system performance and reliability.

3. System description

A process flow diagram of a typical sucker rod pump-driven artificial lift system is shown in Figure 3. It typically consists of a prime mover; a hydrocarbon-powered internal combustion engine (chemical to mechanical energy) or an electricity-powered balanced 3-phase squirrel cage induction motor. The rotational energy from the prime mover is converted by the crank mechanism of the sucker rod into vertical rectilinear reciprocating motion, providing a push motion

in the down stroke and a pull motion in the upstroke, effectively pumping produced fluids to the surface, where it is collected, stored, separated or piped downstream. A typical sucker rod pumping system consists of several key components, each playing a critical role in the overall operation. The surface unit includes the prime mover, gearbox, walking beam, pitman arms, and horsehead, which interact to convert rotational motion into the reciprocating motion needed to drive the rod string. The rod string itself is a series of connected steel or fiberglass rods that transmits this motion to the downhole pump, which includes the pump barrel, plunger, and valves responsible for lifting the fluid to the surface [5] where it is collected, separated, piped and stored accordingly as shown in Figure 3.

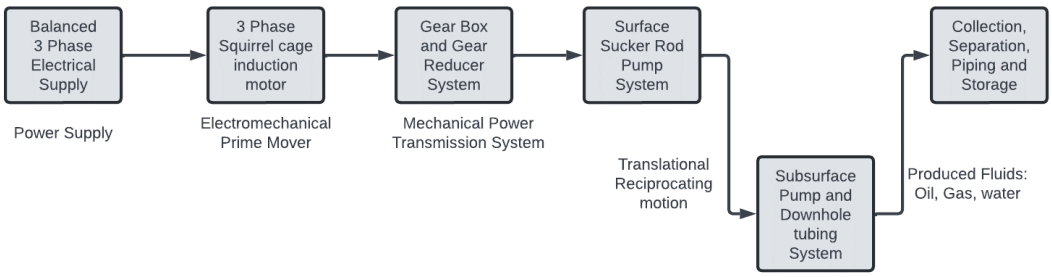

Figure 3. Beam pump system operation and process workflow

4. Methodology

The integration of electrical power supply, power electronics, and mechanical system models within a single simulation environment enables a comprehensive analysis of the system's behavior as shown in Figure 3. This approach allows for the simulation of various operating scenarios and the deployment of optimal control strategies for different conditions. This paper builds on the foundation of previous SolidWorks and Simscape computer-aided design modelling of sucker rod pumps, by developing a detailed model of a sucker rod pump using these advanced simulation tools. The modelling approach encodes the kinematic equations of the walking beam, rod string stress analysis and dynamic load calculations into the surface pumping unit model in Simscape multibody. The gear ratio equations, transmission efficiency and mechanical loss behavior are integrated into the gearbox and gear reducer subsystem, while the rod string subsystem, pump displacement equations, fluid dynamics models, pressure and flow calculations are integrated into the subsurface pump and downhole tubing subsystem. The voltage equations, frequency specifications, and power ratings of the 3-phase electrical supply source subsystem are defined by the equivalent circuits of the 3-phase 100% solar power source which drives the squirrel cage induction machine model. The rotor and stator equations, electromagnetic torque equations, speed-torque characteristics, and machine parameters (resistance, inductance) are integrated into the Simscape model of the squirrel cage induction motor. The oil well powered by a sucker rod pump is modeled as a mechanical load to the squirrel cage induction motor prime mover. Overall, the integrated model in Simscape uses appropriate blocks from the Simscape library: Simscape foundation library, Simscape electrical, and Simscape multibody.

4.1 *Methodology for modelling sucker rod pump in SolidWorks and Simscape*

The geometric model of the sucker rod pump developed and adapted from SolidWorks models is converted to Simscape multibody models using the Simscape multibody link plugin. This process enabled the authors to integrate their CAD assembly with other systems for simulation and analysis in the MATLAB/Simulink environment [15]. The conversion process begins with installing the Simscape multibody link plugin for SolidWorks, the SolidWorks assembly is developed and then exported to an XML file and the corresponding geometry files using the plugin [16]. The XML file is then imported into MATLAB/Simulink to create a Simscape multibody model [17]. The exported model preserves important properties from the SolidWorks assembly: Mass, inertia, and center of gravity of parts are automatically transferred [17]. Assembly

topology and constraints are converted to appropriate joints and constraints in Simscape. The 3D geometry of parts is preserved in the simulation model [17]. This workflow allows for system-level simulation and optimization, integrating mechanical components with electrical, hydraulic, and control systems. It reduces the need for physical prototypes by enabling virtual testing and validation. The authors refined component designs based on accurate system-level requirements [15]. When creating SolidWorks models intended for export, the authors followed certain best practices to ensure clean conversion to Simscape, as they map to specific joint types in Simscape multibody [18].

CAD models from Solidworks are converted in Simulink to Simscape multibody flowcharts using the smimport function, which utilizes XML files to recreate and approximate the original model. The conversion process occurs in two stages: export, where the CAD assembly is converted to XML and geometry files, and import, where these files are transformed into a Simscape multibody model and M-data file [19]. The resulting model obtains all input parameters from the data file, enabling an accurate representation of the original CAD model in Simulink as shown in Figure 4.

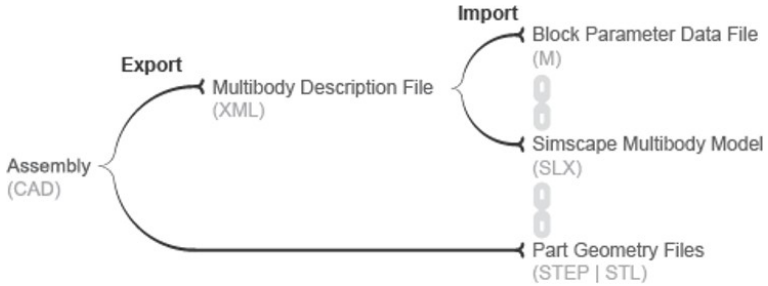

Figure 4. Converting CAD to simscape model [20]

In SolidWorks, the process of creating assemblies relies heavily on the use of mates and constraints to define relationships between components [21]. These elements are crucial in determining how parts interact within the assembly, influencing their relative positions and movements [22]. By accurately defining these relationships, the author ensured that components fit together properly and behave realistically, which is essential when transferring the assembly to simulation environments like Simscape multibody [23]. The precise definition of these connections is vital for maintaining design intent and ensuring the assembly functions as intended in both virtual and physical contexts [22]. The transition from SolidWorks to Simscape multibody involves converting mates and constraints into equivalent joints and constraints within the simulation environment [24]. This conversion process is critical, as different types of SolidWorks mates correspond to specific joint types in Simscape. For example, a concentric mate in SolidWorks might be translated into a revolute joint in Simscape.

The accuracy of the conversions directly impacts the fidelity of the simulation results, influencing the model's behavior under various conditions [25]. Well-constrained models not only facilitate more efficient system-level simulations but also enhance the overall reliability of the analyses performed in Simscape [22]. Smooth transition of models from SolidWorks to Simscape multibody is ensured, by carefully considering and applying appropriate mates and constraints. This thoughtful approach preserves the intended mechanical relationships and behaviors, leading to more accurate simulations and analyses. The quality of the original SolidWorks model, including well-defined mates and constraints, directly correlates with the functionality and accuracy of the resulting Simscape multibody model. This attention to detail in the initial design stages significantly enhanced the overall effectiveness of subsequent simulations and analyses. The foundational SolidWorks model for this research was adapted from earlier work by [26], which presents a SolidWorks model designated as a crank-balance, clockwise, "conventional" beam pump ("C"), with "double-gear" reduction ("D"), maximum torque capacity of 228,000 inch-pounds (in-lbs.), maximum polished rod load of 17,300 pounds (lb), and maximum stroke length of 74 inches.

4.2 *SolidWorks model of sucker rod pump*

Pumping Unit Mechanism: The SolidWorks model includes detailed representations of the surface unit components as shown in Figure 5. Figure 6 shows the Mechanics Explorer view of a Simscape multibody model.

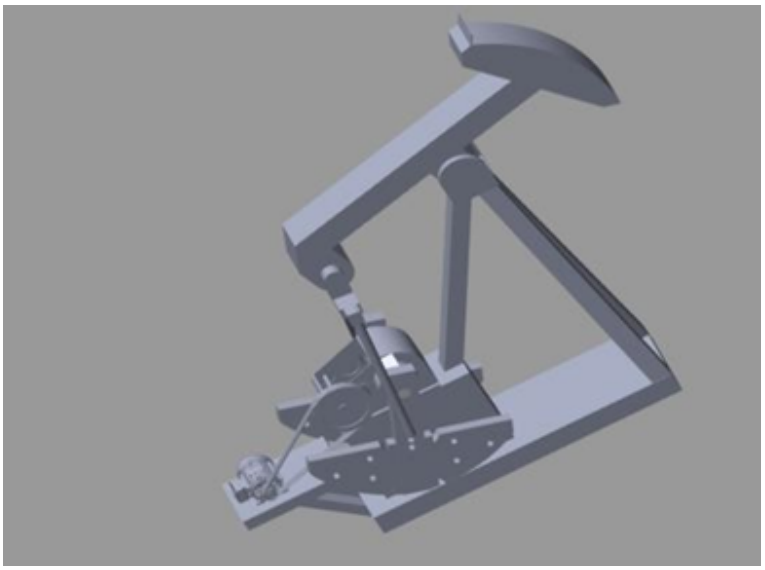

Figure 5. CAD simulation of surface unit

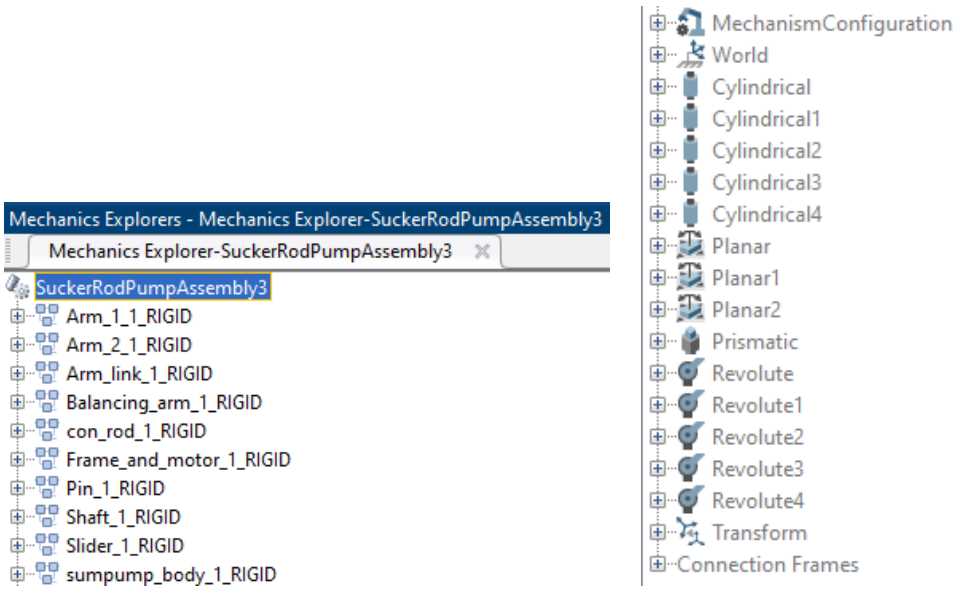

Figure 6. Resolved simscape model showing joints and interactions. (**a**) Rigid bodies. (**b**) Degree of freedom

Figure 6a shows the rigid body elements exported from SolidWorks.

The model elements are SuckerRodPumpAssembly3 which is the main assembly of the sucker rod pump.

Balancing_arm_1_RIGID is a counterbalanced arm, consisting of the horse head and walking beam as shown in Figure 7. Frame_and_motor_1_RIGID is the pump's frame, saddle bearing, Samson post, and motor assembly as shown in

Figure 8. Shaft_1_RIGID is a shaft component connecting the counterbalanced arms as shown in Figure 9. Arm_1_RIGID, and Arm_2_RIGID are the left and right crank and counterweight, rigid bodies representing pump arms as shown in Figures 10 and 11. Arm_link_1_RIGID is made of rigid link connecting arms consisting of the equalizer, equalizer bearing, and pitman as shown in Figure 12. Pin_1_RIGID is a pin which provides a fulcrum for the Con_rod_1_RIGID which is a connecting rod to the sucker rod string as shown in Figure 13. Slider_1_RIGID is the Sucker rod string mechanism. Sumpump_body_1_RIGID is the main body of the downhole submersible pump, consisting mainly of the pump barrel, and standing and traveling valves as shown in Figure 14.

Figure 6b shows the degree of freedom and the mechanical dependency of the rigid bodies from the SolidWorks CAD to the Simscape software environment. The "Mechanism Configuration" defines how the part behaves in a mechanism or assembly. The "World" is the global coordinate system reference. "Cylindrical" (1–5) are cylindrical geometric features or constraints. "Planar" (1–2) are planar surfaces or constraints. "Prismatic" represents a linear motion constraint or feature. "Revolute" (1–4) are rotational motion constraints or features. "Transform" defines the part's position and orientation while "Connection Frames" are points for connecting to other parts in an assembly. This model represents a structured approach for sucker rod pump simulation, allowing for detailed analysis of surface equipment and downhole pump. Its comprehensive nature makes it a valuable tool for oil production engineers and operators in designing, analyzing, and troubleshooting sucker rod pumping systems.

The representation of the subsystem components is defined in (a), (b) and (c) as follows:

(a) Three Dimensional Computer Aided Design (3D CAD) representation of Sucker rod component from Solidworks visualized in the Mechanics Explorer tool in Matlab

(b) Simscape block equivalent of Solidworks component showing the force inputs "F"

(c) Sub-component resolution to fundamental blocks showing coordinate transformations and force relationships in the system

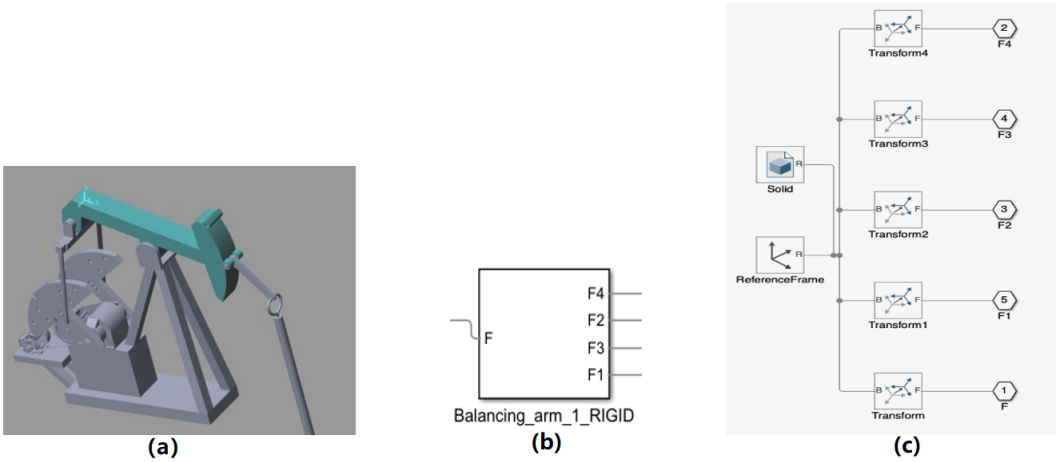

Figure 7. Balancing arm (Balancing_arm_1_RIGID): A counterbalanced arm, consisting of the horse head and walking beam. (**a**) 3D model of Balancing Arm (**b**) Simscape block equivalent of Balancing Arm showing the force input and outputs (**c**) Sub-component resolution of Balancing Arm with fundamental blocks showing coordinate transformations and force relationships in the system

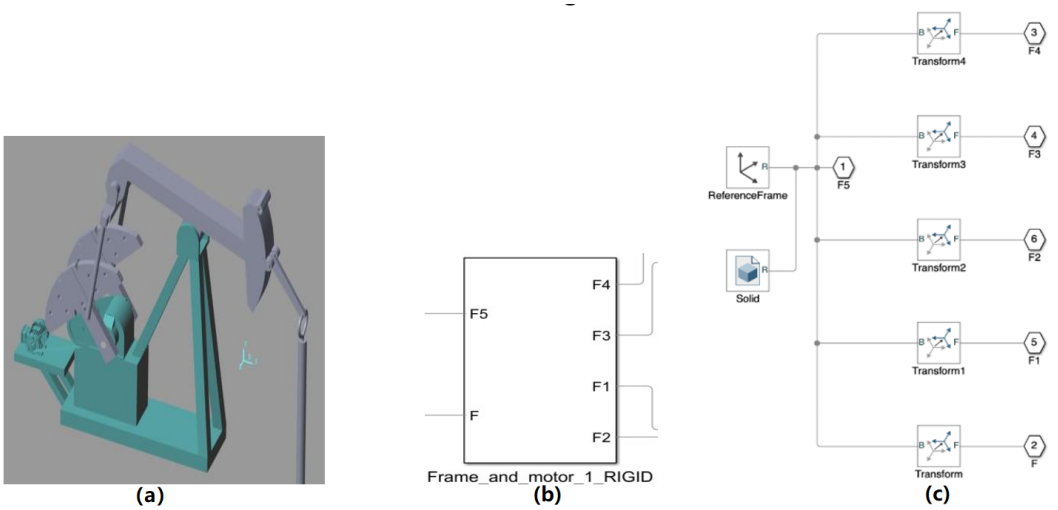

Figure 8. Frame and motor (Frame_and_motor_1_RIGID): The samson post, pump's frame, and motor assembly. (**a**) 3D model of Samson post, pump's frame, and motor assembly (**b**) Simscape block equivalent of Samson post, pump's frame, and motor assembly showing the force input and outputs (**c**) Sub-component resolution of Samson post, pump's frame, and motor assembly with fundamental blocks showing coordinate transformations and force relationships in the system

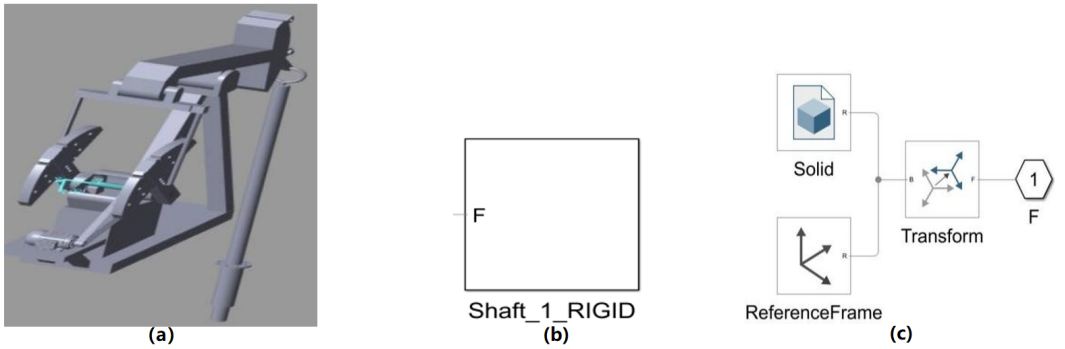

Figure 9. Shaft 1 rod (Shaft_1_RIGID): A shaft component. (**a**) 3D model of shaft Rod (**b**) Simscape block equivalent of shaft rod showing the force input and outputs (**c**) Sub-component resolution of Shaft Rod with fundamental blocks showing coordinate transformations and force relationships in the system

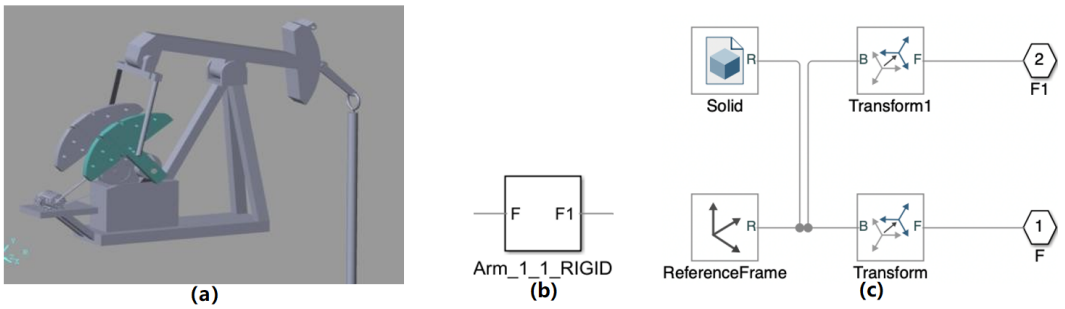

Figure 10. Arm 1. Arm_1_RIGID (Arm 1): A Crank and Rotary counterbalance Arm (first). (**a**) 3D model of a crank and rotary counterbalanced arm (**b**) Simscape block equivalent of crank and rotary counterbalanced arm showing the force input and outputs (**c**) Sub-component resolution of crank and rotary counterbalanced arm with fundamental blocks showing coordinate transformations and force relationships in the system

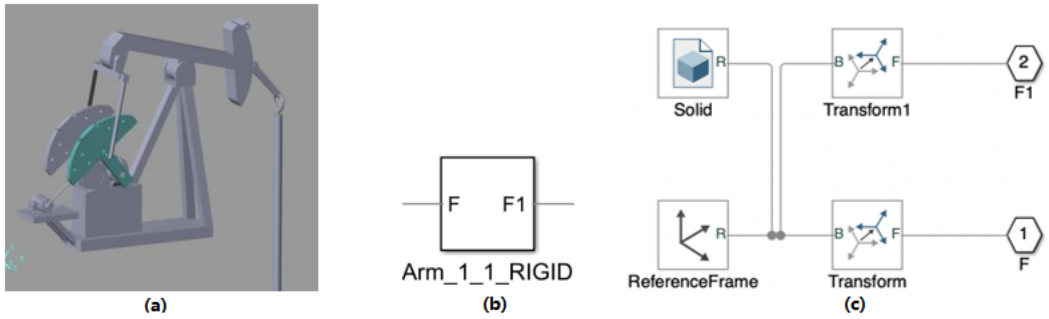

Figure 11. Arm 2 (Arm_1_RIGID, Arm_2_RIGID): Rigid bodies representing pump arms: Crank and counterweight. Arm_2_RIGID (Arm 2): A Crank and Rotary counterbalance Arm (second). (**a**) 3D model of the crank and rotary counterbalanced arm (**b**) Simscape block equivalent of the crank and rotary counterbalanced arm showing the force input and outputs (**c**) Sub-component resolution of the crank and rotary counterbalanced arm with fundamental blocks showing coordinate transformations and force relationships in the system

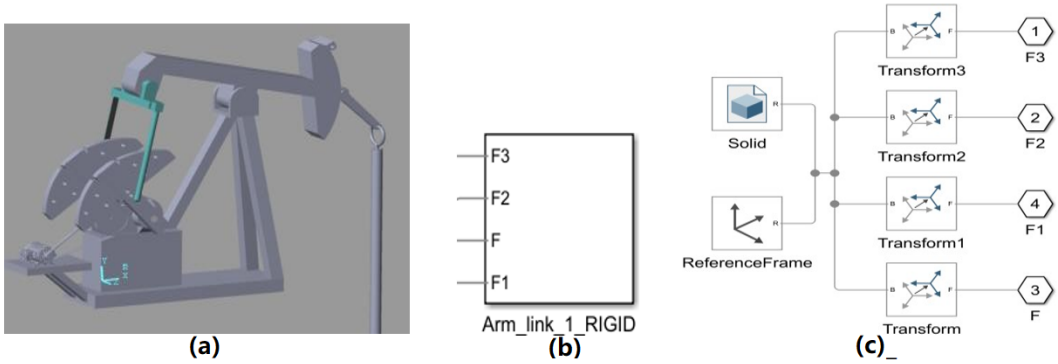

Figure 12. Arm link 1 RIGID (Arm_link_1_RIGID): A rigid link connecting arms consisting of the equalizer, equalizer bearing, and pitman. (**a**) 3D model of an arm link (**b**) Simscape block equivalent of arm link showing the force input and outputs (**c**) Sub-component resolution of arm link with fundamental blocks showing coordinate transformations and force relationships in the system

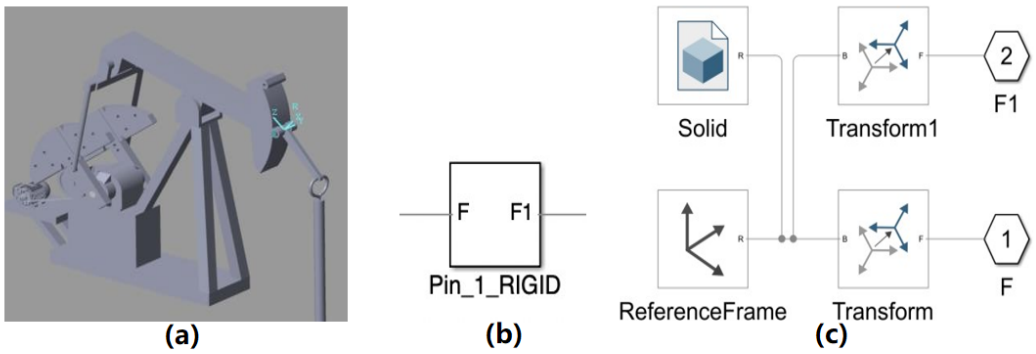

Figure 13. Pin 1 rod (Pin_1_RIGID): A pin joint. Pin 1 rod (Pin_1_RIGID): A pin fulcrum for the connecting rod. (**a**) 3D model of a pin fulcrum (**b**) Simscape block equivalent of pin fulcrum showing the force input and outputs (**c**) Sub-component resolution of pin fulcrum with fundamental blocks showing coordinate

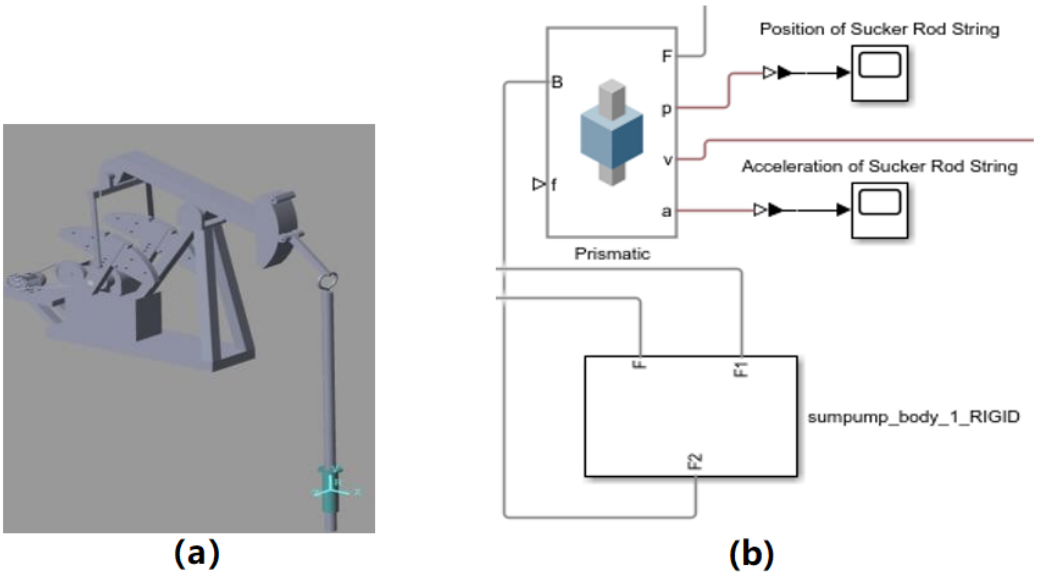

Figure 14. Down hole pump rigid (sumpump_body_1_RIGID): The main body of the sump pump. (**a**) 3D model of the main body of the subsurface pump (**b**) Simscape block equivalent of the subsurface pump showing the force input and outputs (**c**) Sub-component resolution of the subsurface pump with fundamental blocks showing coordinate transformations and force relationships in the system

4.3 *Detailed analysis of model-based subsystems*

(i) **Prime mover**: A balanced 3-phase induction motor is modeled in Simscape electrical machines. The Squirrel cage induction motor model uses an asynchronous machine squirrel cage (fundamental) block from the Simscape electrical library to represent the balanced 3-phase induction motor. The induction motor was modeled first in Simscape electrical and then modeled again to simulate integration with the overall circuit in Simscape Power systems, the initial parametrization of the induction motor has been included in Figure 15a based on a previous work by the authors in [27], while the full motor parameters and nameplate data are presented in Table 8. The equivalent circuit parameters for the squirrel cage induction motor are presented in Figure 15a and the squirrel cage induction motor model and its integration into the sucker rod pump system is presented in Figure 15b.

The Squirrel cage induction motor is a common choice for most sucker rod pumps due to its robustness, efficiency, and ability to handle the cyclic loading characteristic of these systems [5]. The three-phase supply (ports a_1, b_1, c_1) represents the three-phase power input to the motor, which is standard for industrial applications due to its efficiency and smooth power delivery [5]. The wye configuration (ports a_2, b_2, c_2) connected to electrical reference (ground), is common in oil field applications as it provides a good balance of voltage and current characteristics [27]. Mechanical output (port R) is connected to the gearbox, providing the rotational mechanical power to drive the pumping unit. Case connection (port C) connected to the mechanical rotational reference, represents the motor's fixed mounting, which is crucial for proper torque transfer.

(ii) **Gearbox and Gear Reducer System**

This system is modeled in Simscape multibody. It receives input angular velocity from the prime mover and outputs torque to the sucker rod pump. If the angular velocity ω of the mating gear is constant, then n, d and T are the gear speed, diameter, and the number of teeth, while 1 and 2 are the driver and driven gears respectively [29].

$$Gear\ ratio = \frac{\omega_1}{\omega_2} = \frac{n_1}{n_2} = \frac{d_2}{d_1} = \frac{T_2}{T_1} \tag{1}$$

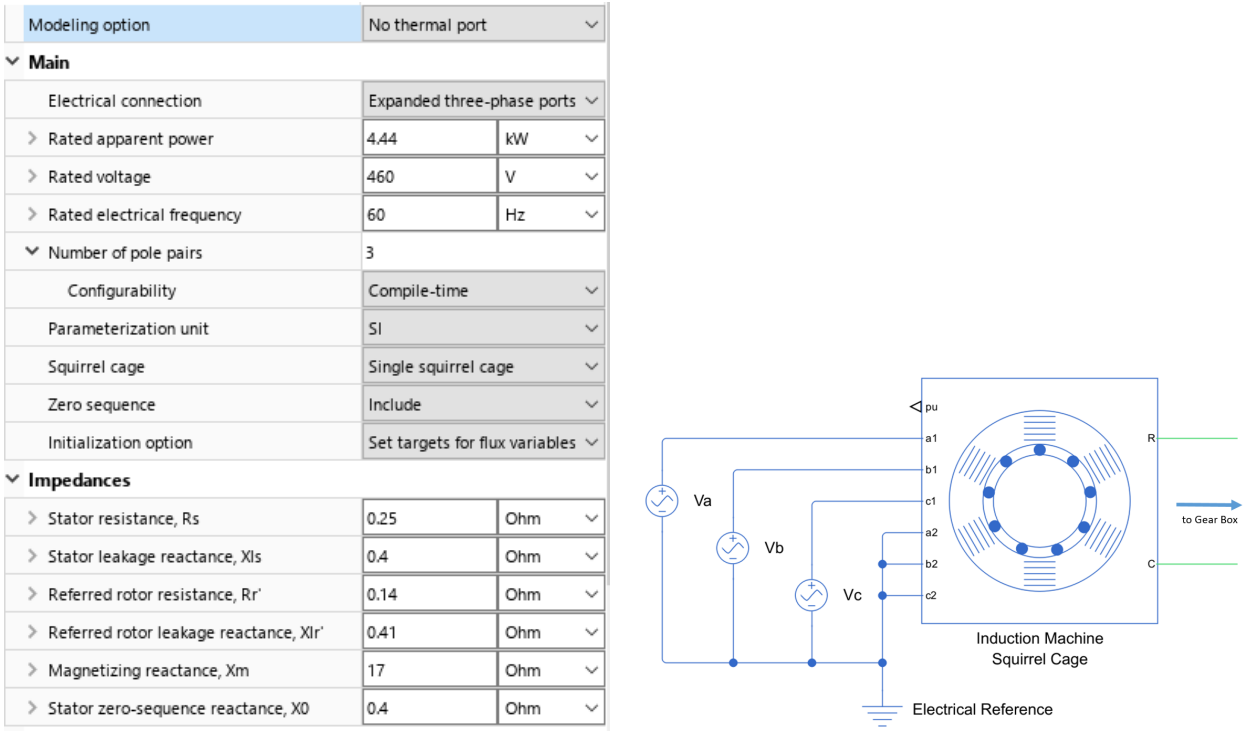

Figure 15. (**a**) Equivalent circuit parameters, (**b**) Three-phase electric motor in simscape

An equivalent representation of the Simscape model of the gearbox subsystem for a sucker rod pump is shown in Figure 16a. Gearbox block represents the physical gearbox in a sucker rod pumping unit. In actual systems shown in Figure 16b, the gearbox (also called speed reducer) is crucial for converting the high-speed, low-torque output of the prime mover (electric motor) into the low-speed, high-torque input required by the crank [5]. The gearbox uses a worm gear arrangement for its high reduction ratio, enabling it to handle the cyclic loading characteristic of sucker rod pumps. Port S represents the input shaft connection from the prime mover, while Port O stands for the Output shaft connection to the crank. The rotational multibody interface serves as an interface between the 1D rotational domain (gearbox) and the 3D multibody domain (pumping unit mechanism). It is essential for accurately translating the rotational motion and torque from the gearbox to the rest of the pumping unit model. Port W is the angular velocity input, while T is the torque input, R is the rotational frame connection, and C is the connection to the 3D multibody system (which represents the Crank). The spring-damper icon models some compliance and damping in the connection, which is important for capturing the dynamic behavior of the system. Mechanical rotational reference provides a fixed reference frame for the rotational components, essential for defining the absolute motion of the system [30, 31].

Key aspects of this model are power transmission, speed reduction, the interface between domains, and power transmission for dynamic behavior. The model accurately represents the power flow from the prime mover through the gearbox to the pumping unit mechanism. This is crucial for analyzing the efficiency of power transmission and the loads on various components for speed reduction. At the same time, the gearbox model allows for the simulation of speed reduction, which is vital in sucker rod pump operations [5]. As an interface between domains, the rotational multibody interface is a sophisticated element that bridges the gap between simplified one-dimensional rotational dynamics and complex three-dimensional multibody dynamics. This is crucial for accurately simulating of the entire system and for studying the dynamic behavior. The inclusion of compliance and damping (represented by the spring-damper icon) allows for the modelling of dynamic effects such as torsional vibrations, which can be significant in sucker rod pumping systems [32].

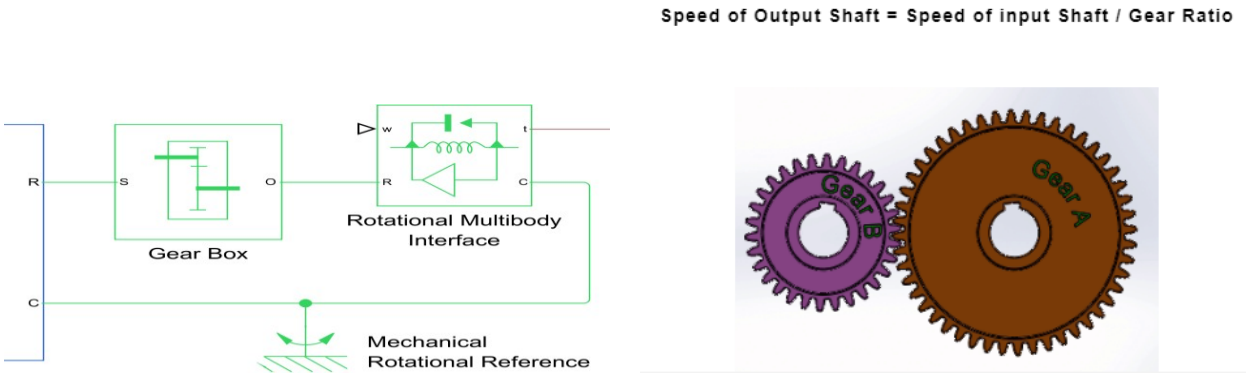

Figure 16. (**a**) Gearbox and gear reducer system, (**b**) Gear reduction [29]

The gearbox output directly influences the motion of the sucker rods and downhole pump. Accurate modelling here is essential for predicting downhole pump behavior. The gear ratio affects pumping speed, which directly impacts fluid dynamics in the downhole pump and wellbore. The gearbox's performance influences load distribution along the entire rod string, affecting stress on downhole components and proper gearbox modelling is crucial for optimizing overall system efficiency, including downhole pump performance.

(iii) **Sucker rod surface pumping unit**: Correlating each element to its physical counterpart, a detailed analysis of the Simscape model of the sucker rod pump and rod string system is shown in Figure 17.

Correlating each element to its physical counterpart, "World" and "Transform" blocks establish the global reference frame and coordinate transformations, essential for accurately positioning components in 3D space. Frame_and_motor_1_RIGID represents the pump's structural frame and prime mover (a 3-phase electric motor). This is the foundation of the surface equipment. Revolute joints (Revolute, Revolute1, Revolute2, Revolute3) simulates the rotational connections in the pumping unit, such as Crank-Frame connection, Crank-Pitman connection, Pitman-Walking beam connection, Walking beam-Stand connection, Arm_2_1_RIGID, Arm_1_1_RIGID, Arm_link_1_RIGID represent the pump arms: crank and counterweight, and rigid link connecting arms consisting of equalizer, equalizer bearing, and pitman. Balancing_arm_1_RIGID simulates the counterweight system, a counterbalance arm, consisting of the horse head and walking beam, which balances the sucker rod string load and reduces peak torque requirements. Cylindrical joints (Cylindrical, Cylindrical1, Cylindrical2, Cylindrical3, and Cylindrical4) represent connections that allow both rotational and translational motion, such as where the pitman connects to the crank and walking beam. Planar and Planar1, Planar2 constrain motion to a plane, used to ensure components move in the correct 2D plane of the pumping unit. The prismatic joint represents a sliding connection, simulating the motion of the sucker rod string within the tubing. Shaft_1_RIGID represents the polished rod, which connects the surface equipment to the sucker rod string. Pin_1_RIGID represents a connection point, where the horse head connects to the walking beam. Con_rod_1_RIGID represents the bridle (wireline hanger), bridle block, and carrier bar, which connect the horse head to the polished rod. Slider_1_RIGID represents the polished rod that translates translational reciprocating motion from the surface to the downhole pump. Sumpump_body_1_RIGID represents the main body of the pumping unit, providing structural support [30, 33].

(iv) **Subsurface pump and downhole tubing**

In analyzing the Simscape model of the downhole pump of the sucker rod pump system, each element is correlated to its physical counterpart in a downhole pump setup as shown in Figure 18.

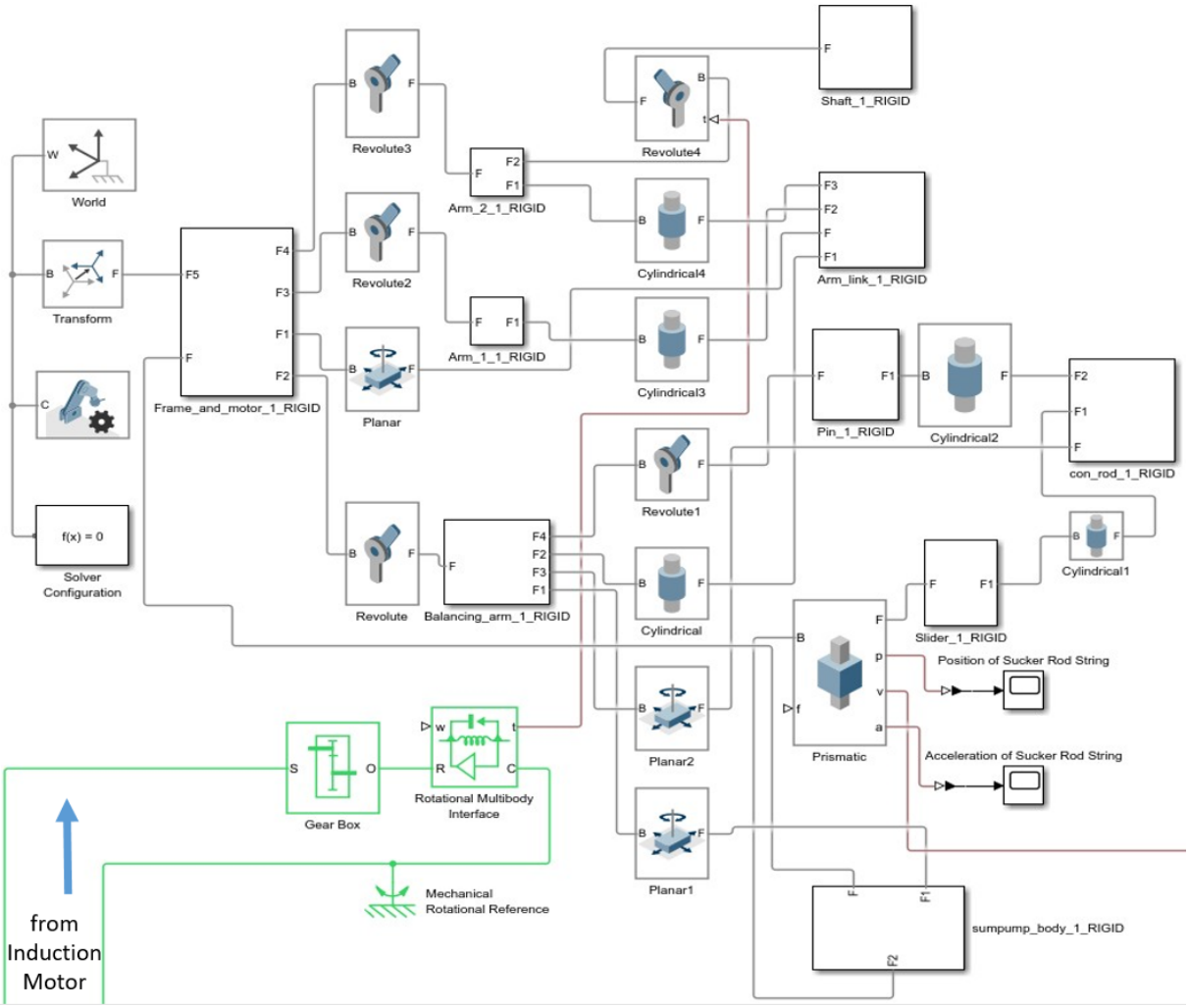

Figure 17. Model of surface pumping unit (connected to gearbox and gear reducer system)

The constant head tank represents the underground oil reservoir. While real reservoirs experience pressure depletion over time, for short-term modelling, constant pressure is often assumed. This simplification is common in nodal analysis of production systems. The pressure here corresponds to the bottom hole flowing pressure (P_{wf}) in an actual well. Double-acting hydraulic cylinder simulates the pump barrel and plunger assembly. The lower chamber represents the volume below the plunger, while the upper chamber represents the volume above it.

The Visual representation of the operating principles of a sucker rod pump is shown in Figure 19. Two check valves are crucial in the model, the standing valve and the traveling valve. The Standing valve (lower) located at the bottom of the pump, allows fluids to enter the barrel from the reservoir but prevents backflow. The traveling valve (upper) attached to the plunger allows fluid migration from below the plunger to above it during the down stroke and prevents backflow during the upstroke. These valves are fundamental to the operation of sucker rod pumps and are accurately represented in the model [28].

The ideal translational velocity source generates the velocity input for the plunger motion, simulating the reciprocating movement induced by the surface pumping unit. It is proportional to the polished rod velocity at the surface. This simplification is reasonable for basic modelling but doesn't account for harmonics and damping effects in the rod string. Variable Head Two-Arm Tank represents the tubing string and surface pressure conditions. The fluid column in this tank simulates the hydrostatic pressure in the production tubing. This dynamic representation is crucial for accurately modelling

the changing back pressure during pumping cycles. Resistive Pipe LP1 represents the flow resistance in the production tubing, accounting for friction losses [28].

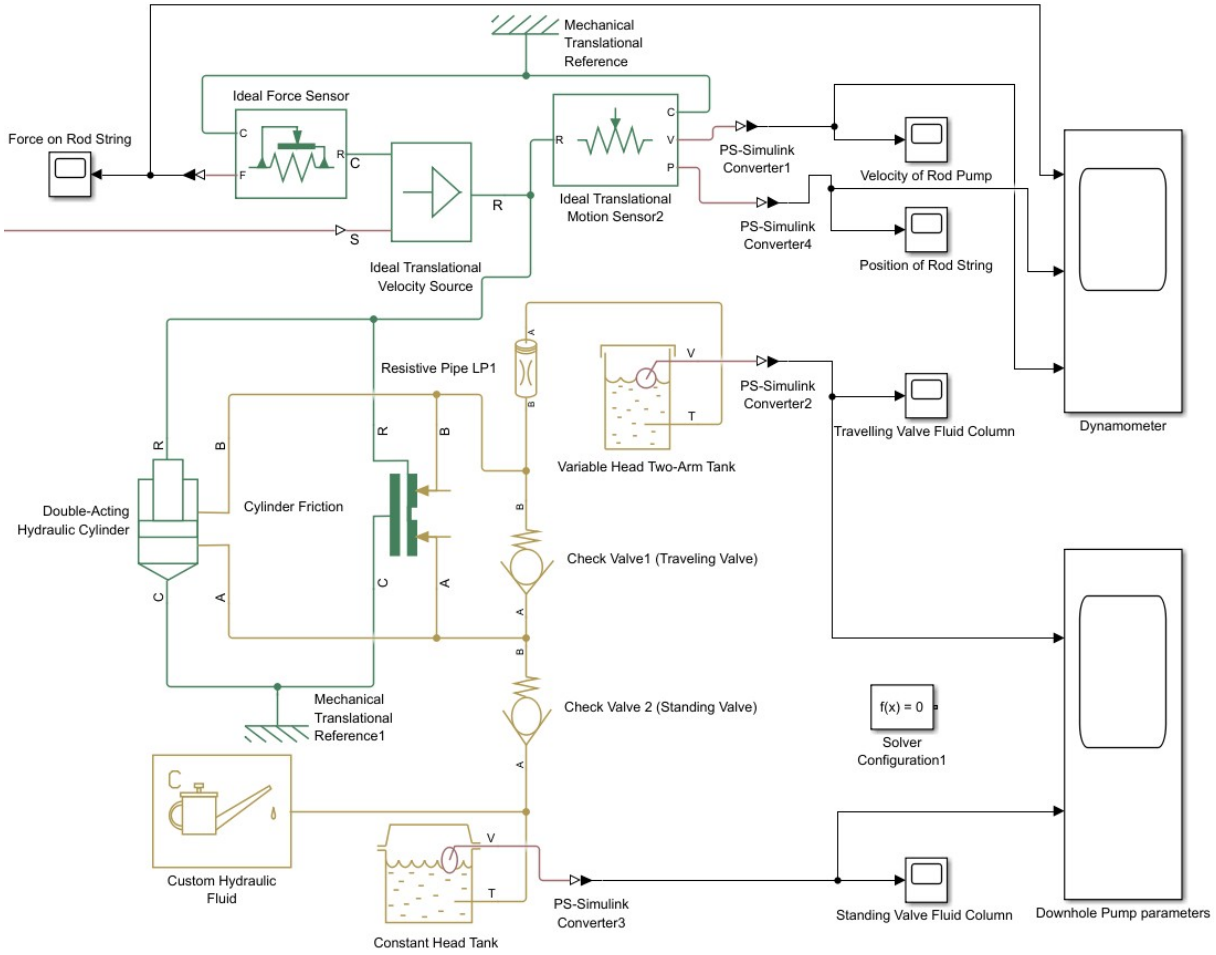

Figure 18. Model of submerged pump barrel assembly including metering and instrumentation devices [28]

During the upstroke, the standing valve opens as the plunger moves up, creating a pressure differential that allows fluid to enter the pump barrel from the reservoir. Simultaneously, the traveling valve closes, allowing the fluid above it to be lifted towards the surface. On the down stroke, the standing valve closes to prevent fluid from flowing back into the reservoir. The traveling valve opens, allowing fluid to pass through the plunger, positioning it for the next upstroke. This operation closely mirrors the actual functioning of sucker rod pumps as described in the literature [5].

This Simscape model provides a comprehensive representation of the sucker rod pump's operation, allowing simulation of various operating conditions, ensuring robust analysis of pump performance, and optimizing production parameters. The model effectively considers the key dynamics of a sucker rod pumping system. However, it is important to note that while this model captures many essential aspects of beam pump operation, real-world complexities such as gas interference, sand production, or complex fluid behaviors in the wellbore are beyond the scope of this model.

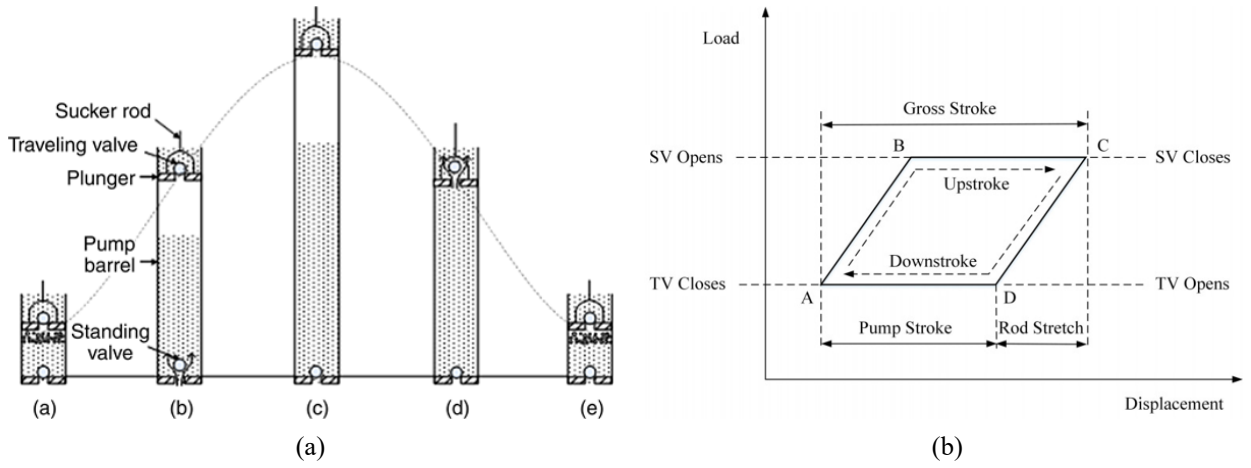

Figure 19. Visual representation of the operating principles of a sucker rod pump. (**a**) The pump stroke cycle of the downhole pump. (**b**) Load/displacement dynamics

4.4 *Methodology for modelling solar-powered sucker rod oil pump*

The methodology for modelling a solar-powered sucker rod pump combines the estimated load rating of the sucker rod pump from previous work by the author in [14], with the subsequent feasibility study on optimal sizing, technical and economic analysis of a renewable power system for a remote oil well [27]. A renewable energy microgrid consisting of a solar-powered sucker rod oil pump is designed, modeled, simulated, and controlled in Simulink/Simscape. The selected site is near Medicine Hat, a city in Southeast Alberta, Canada. Latitude 50°2′32″ N and longitude 110°48′49″ W. Like most of the Prairies, there is an abundance of idle and inactive wells that have been suspended, orphaned, and abandoned in this area, most of which are significantly remote and do not have access to the power grid.

Typical solar irradiation for the area is 3.61 kWh/m^2/day, the average estimated daily electrical demand is 2.59 kW, with a peak demand of 4.44 kW [27].

5. PV system design

The schematic of the proposed system is presented in Figure 20. It consists of the Solar PV array, DC/AC inverter, battery storage, and the induction motor, with an associated step-up transformer for voltage transformation. In the previous research by the author [27], the technical and economic feasibility of sizing a 100% solar-powered system with battery storage was extensively studied in hybrid optimization of multiple energy resources (HOMER Pro) software.

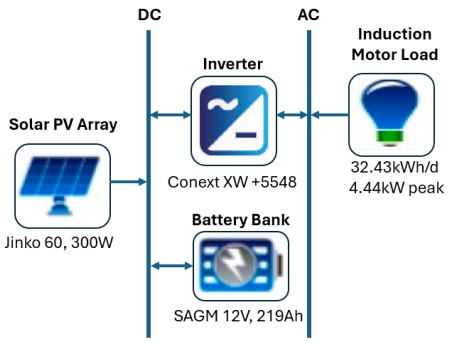

Figure 20. Schematic diagram of the proposed system

The conclusion from comparing various scenarios with continuous and intermittent pumping configurations using several criteria including net present cost, levelized cost of energy, total production, consumption, and excess electricity, is that continuous pumping with hybrid generation (solar PV, wind and battery storage) has the least unmet load and capacity storage with 0 kWh/yr of unmet load, capacity storage of 0.56 kWh/yr, a net present cost of $145,150.50, a levelized cost of energy of $0.51/kWh and an operating cost of $3056.04/yr; while intermittent pumping configuration with solar PV and battery system with 4.55 kWh/yr of unmet load, capacity storage of 11.70 kWh/yr, a net present cost of $64,969, a levelized cost of energy of $0.425/kWh and an operating cost of $1318/yr. Intermittent pumping with solar PV and battery system will be the chosen configuration for further design in this research because considering production from inactive oil wells (suspended and idle), the unmet load for the solar PV and battery system can be suitably accommodated in the pumping schedule as a trade-off to the significantly reduced cost in comparison to the solar PV, wind and battery storage system. Hence the solar PV and battery system would be adopted for powering the remote oil well. The system proposed by the author in [27] comprises a 27.3kW Solar PV array, and battery bank, comprising 64 units of deep cycle batteries, of 16 strings and 4 batteries per string. A system converter rated 4.49 kW and a load dispatch of cycle charging is implemented, implying that the primary load (electric motor) receives supply first and the excess generation goes to charge the battery bank. The elements and parameters of the solar PV supply are defined in Table 1, as defined in the previous design and feasibility study by the authors [27].

Table 1. Solar microgrid source

Component	Name	Size
PV	Jinko eagle PERC60	27.3 kW
Storage	Deep cycle batteries, SAGM (12 V, 219Ah)	64 units (16 strings)
System converter	Schneider (Conext XW + 548)	4.49 kW
Dispatch	Cycle charging	

To analyze the system performance, robustness, and resilience under different environmental conditions, the average solar irradiance data obtained in January for winter and June for summer are extracted from the open-source Canadian Weather Energy and Engineering Climate (CWEC) data at [34] from the official website, and the average hourly daily temperatures are also available from [35, 36]. This research makes a novel contribution in considering the response of the system to varying environmental factors and changes in operational conditions, by performing parallel simulations of the key performance indicators for a "representative" or sample winter and summer months, January for winter and June for summer. The average solar irradiance and temperature data for summer and winter are respectively given in Tables 2 and 3. The plot of the hourly solar irradiance data is presented in Figure 21a,b.

Table 2. Average solar irradiance and temperature data for winter at Medicine Hat [34, 35]

Time (Hrs)	Irr (W/m^2)	Temp (Deg. C)
1	0	−7
2	0	−8
3	162	−8
4	752	−8
5	1239	−7
6	1548	−6
7	1657	−6
8	1558	−5
9	1260	−6
10	781	−7
11	198	−8
12	0	−9

Table 3. Average solar irradiance and temperature data for summer at Medicine Hat [34, 36]

Time (Hrs)	Irr (W/m^2)	Temp (Deg. C)
1	0	10
2	138	10
3	785	10
4	1513	12
5	2236	15
6	2904	19
7	3472	22
8	3900	23
9	4160	25
10	4234	25
11	4117	25
12	3817	27
13	3354	27
14	2760	27
15	2075	27
16	1347	27
17	624	26
18	60	24
19	0	21

Considering the data available from Tables 2 and 3 and the plots in Figure 21a,b, and scaling the data accordingly for 1 h $\equiv$ 1 s for simulation, we can infer that there is significantly higher average hourly irradiance and correspondingly higher temperatures for the chosen location in the summer months than in winter.

Figure 22 shows the equivalent circuit diagram for the design, dynamic modelling, simulation, and control of a solar-powered sucker rod oil pump. The same system equivalent circuit design and model are adopted for summer and winter, with the output power wholly dependent on the daily solar irradiance and ambient temperature as shown in Tables 2 and 3, and Figure 21. The block diagram of the proposed system is shown in Figure 23.

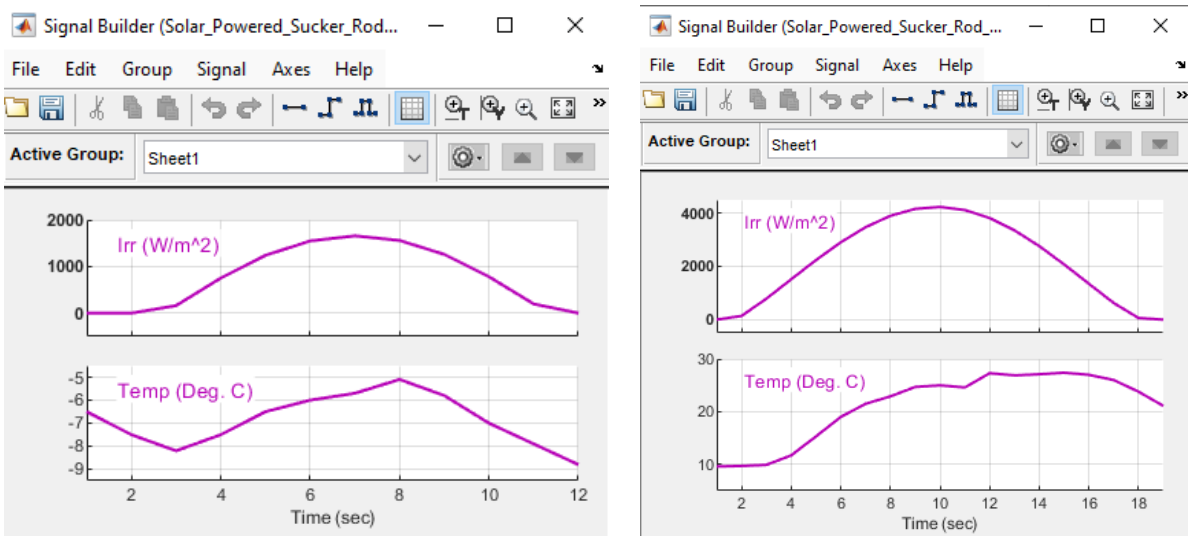

(a) (b)

Figure 21. Sample average daily solar irradiance and temperature data for Medicine Hat for winter and summer respectively. (**a**) Sample winter data (January). (**b**) Sample summer data (June)

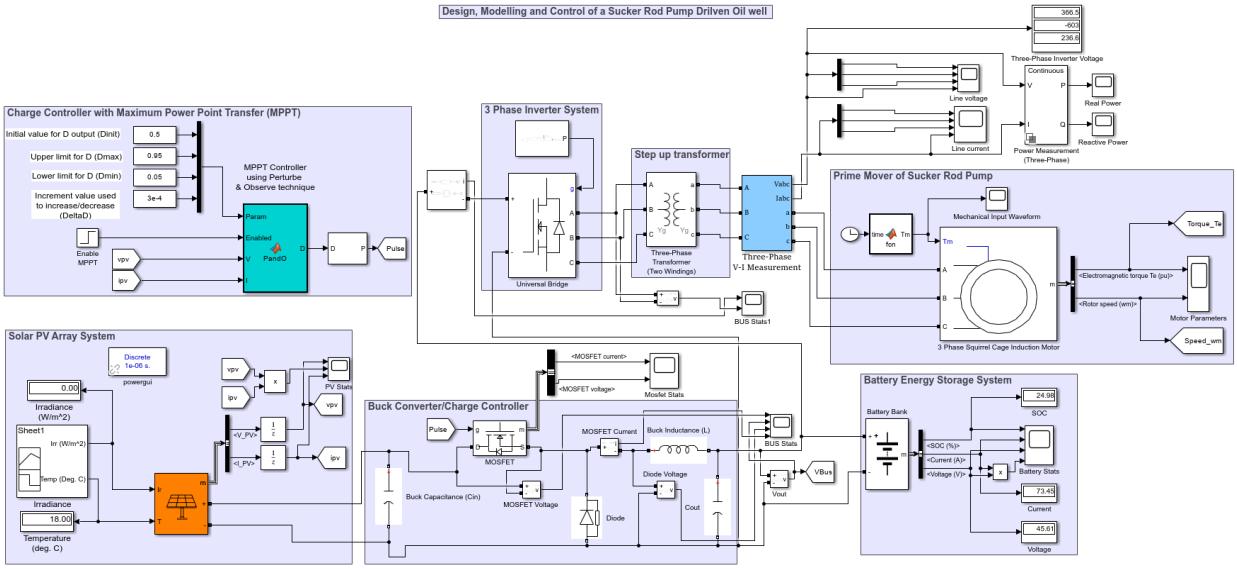

Figure 22. Circuit diagram showing subsystems modeled to achieve 100% microgrid

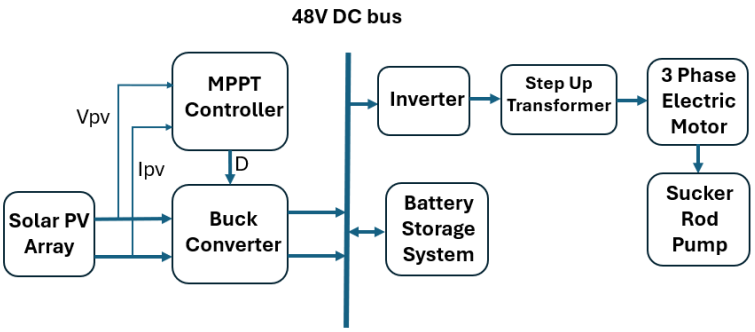

Figure 23. Block diagram of proposed solar PV microgrid

5.1 *Solar PV system*

The solar photovoltaic system consists of several modules combined in required numbers and configurations to generate sufficient direct current power from the solar irradiance received. To attain the required power configuration, the PV modules could be connected in series to form strings, this leads to an increase in the resulting voltage, while the current remains the same. Multiple strings could also be connected together to form solar PV arrays, leading to an increase in current while the voltage remains the same. There are several types of solar cells for PV systems, and this affects the behavior, performance, and efficiency of the resulting PV array. Environmental factors such as the ambient temperature and solar irradiance also affect the performance of selected modules as shown by the Current-Voltage (I–V) and Power-Voltage (P-V) curve of the 60-cell, 300W PV module in Figure 24.

The PV cells selected for this study are Passive Emitter and Rear Contact (PERC), a new technology designed to achieve a (1–2)% higher energy conversion efficiency, due to the added dielectric passivation layer on the cell's rear. To determine the I-V and P-V characteristics curve, the PV cell's output current I_{PV} is given by Kirchhoff's current law as Equation (2).

$$I_{PV} = I_{ph} - I_D - I_{sh} = I_{ph} - I_O \left[\exp\left\{ \frac{q(V_{PV} + R_s I_{PV})}{nkT} \right\} - 1 \right] - \frac{(V_{PV} + R_s I_{PV})}{R_{sh}} \quad (2)$$

where I_{ph}, I_D, and I_{sh} represent photogenerated current which increases with light intensity, diode current that accounts for internal recombination losses and leakage current across shunt resistance of parallel paths respectively. I_O is the reverse saturation current, n is the diode ideality factor, q is the elemental charge, k, Boltzmann constant, T, absolute temperature (K), where, R_s and R_{sh} are series resistance (preferably very small) and shunt resistance (preferably very large) as shown on the equivalent circuit of the solar PV cell in Figure 25.

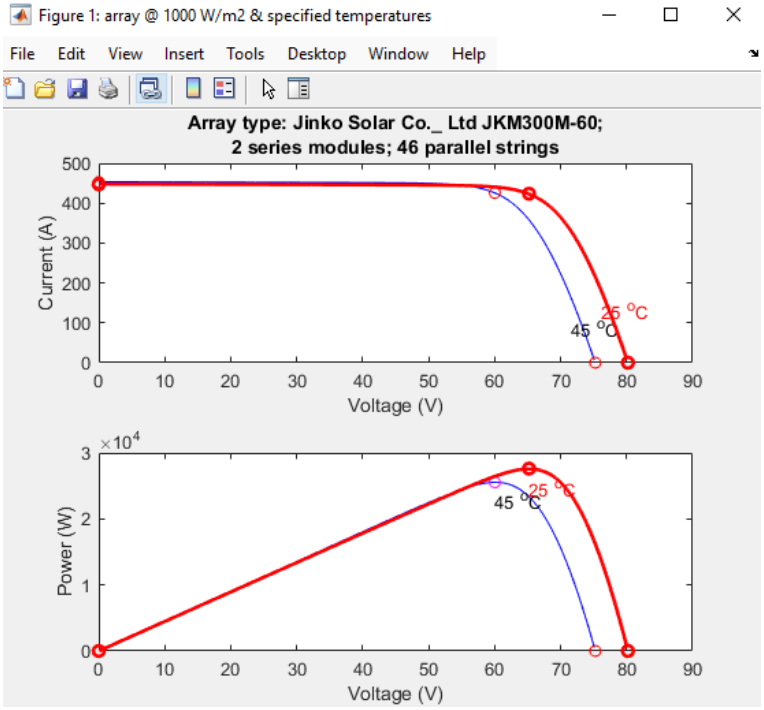

Figure 24. Output power and current of the PV versus voltage

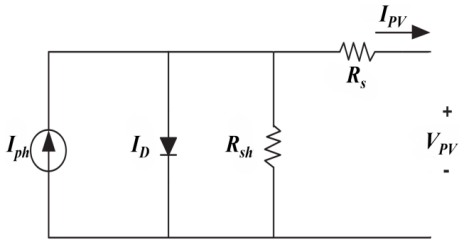

Figure 25. Equivalent circuit model of single PV cell

To obtain the required DC bus voltage (48 V) and the target power of the array (27.3 kW), we consider the number of parallel strings and the number of series-connected modules per string. Each 60-cell solar panel has a voltage at a maximum point V_{mpp} of 32.6 V, sufficient for reliably charging a 24 V battery system, which needs over 30 V to charge. The system uses two 60-cell solar panels connected in series. Given a PV rating of 27.3 kW, and a maximum power per module of 300 W. The total number of solar PV panels required is theoretically 27.3 kW divided by 300 W which equals 91. Using an average of 24 V per panel and series-connected modules per string N_s of 2 (panels in series), we have a minimum series voltage (V_{in-min}) of 48 volts, and given V_{mpp} of 32.6, we get a maximum series voltage (V_{in-max}) of ~66 V. The range of output voltage for the PV system is thus (48–66) V. Given 2 series-connected modules per string and 91

panels, the number of parallel string pairs N_p will be 91 divided by 2, which is ~ 46. Given a PV rating of 27.3 kW, and a minimum series voltage (V_{in-min}) of 48.

From the Array specifications in Figure 26, we can infer that the theoretical maximum power that can be reliably extracted from the solar PV array is given by Equation (3) [37]:

$$\begin{aligned} P_{mpp} &= (N_p \times I_{mpp}) \times (N_s \times V_{mpp}) \\ &= (46 \times 9.21) \times (2 \times 32.6) \approx 27.6 \text{ kW} \\ &= \text{Total Number of modules} \times \text{Maximum Power per module} \\ &= 46 \text{ parallel strings} \times 2 \text{ modules per string} \times 300.246 \text{ W} \\ &\approx 27.6 \text{ kW} \end{aligned} \tag{3}$$

The Solar PV array design specifications for modelling are given in Figure 26. The parameters for the design and sizing of the Solar PV source are presented in Table 4.

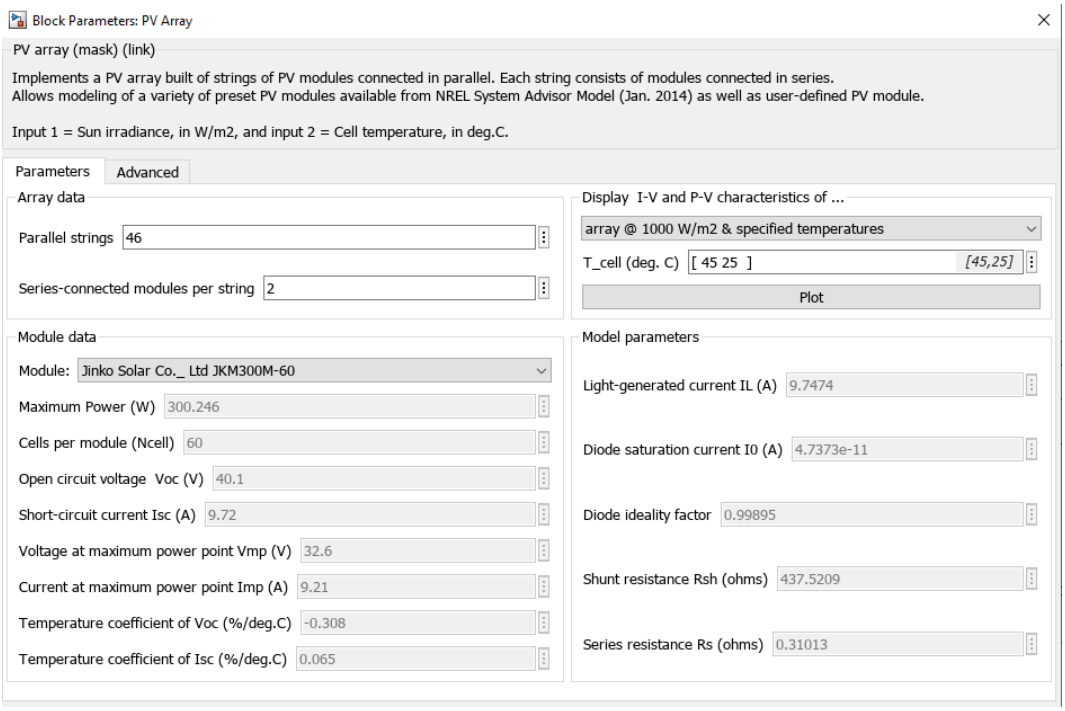

Figure 26. Solar PV array design specifications for modelling

Table 4. Showing solar PV system parameters

System parameters	Ratings	Unit
Module peak power of a single module (P_{mp})	300.25	W
Module open circuit voltage (V_{oc})	40.1	V
Module short circuit current (I_{sc})	9.72	A
Module voltage at MPP (V_{mp})	32.6	V
Module current at MPP (I_{mp})	9.21	A
Array peak power (P_{mp})	27.6	kW
Array open circuit voltage (V_{oc})	80.2	V
Array short circuit current (I_{sc})	447.12	A
Array voltage at MPP (V_{mp})	65.2	V
Array current at MPP (I_{mp})	423.66	A

5.2 *DC-DC buck converter*

DC-DC converters are essential components in photovoltaic systems, acting as intermediaries that optimize power transfer through impedance matching. These devices enable maximum power point tracking by dynamically adjusting their duty cycles, allowing the system to operate at its most efficient point on the current-voltage characteristic curve. The buck converter stands out as a particularly effective topology when DC voltage reduction is needed between source and load. This makes it especially suitable for systems where PV module output voltage exceeds battery charging requirements as in this design. From Figure 27, when the switch activates, the output capacitor begins charging, the inductor regulates the current flow, creating a controlled charging process, and the capacitor voltage rises gradually throughout each switching cycle. This configuration enables efficient voltage step-down while maintaining stable output characteristics, making it ideal for renewable energy applications where precise voltage control is crucial for system performance. The bus voltage is 48 V, and the range of output voltage for the PV system is (48–66) V hence a buck converter is required. Where V_{in-min} and V_{in-max} are minimum and maximum input voltages, V_{out} and I_{out} are output voltage and currents, f is the switching frequency, and V_{in} is the sample input voltage. Given the transfer function of a Buck converter from [38] where $V_{out} = 48\ V$, $V_{in} = 66\ V$, minimum input capacitance used $C_{in} = \ 4740\ \mu F$, minimum inductor value is $L_{Buck} = 17.319\ \mu H$, while the output capacitance $C_{Out} = \ 5924.48\ \mu F$. The output voltage is held constant at 48 V, while the input voltage from the PV array at MPPT ~ 66 V. The equivalent circuit diagram of the buck converter design is shown in Figure 27. The parameters for the design and sizing of the charge controller implemented as a DC-DC buck converter are presented in Table 5.

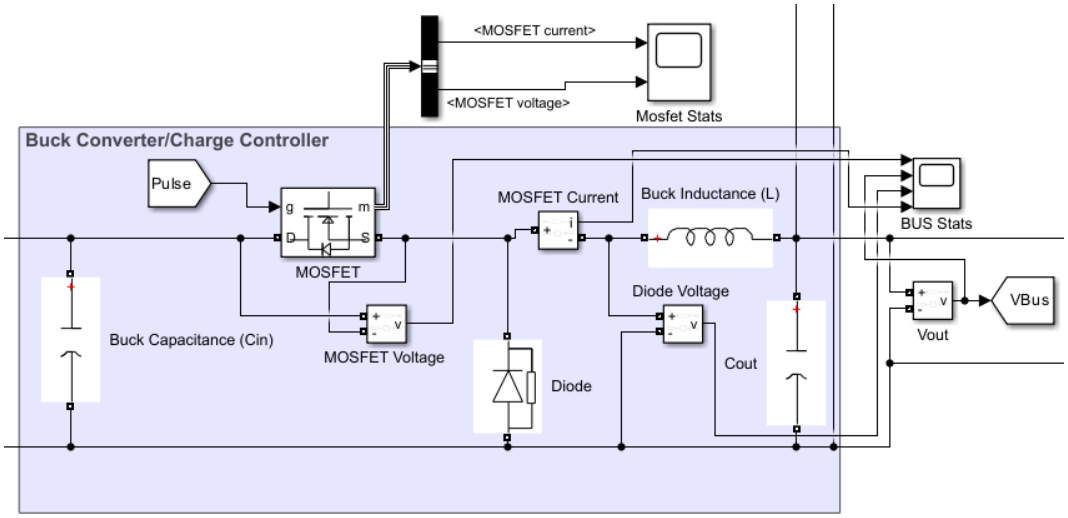

Figure 27. Equivalent circuit of buck converter for charge control and MPPT implementation

Table 5. Showing buck converter system parameters

System parameters	Ratings	Unit
Input voltage at MPPT (V_{in})	66	V
Frequency (f)	5	kHz
Buck inductance (L_{Buck})	17.32	µH
Buck capacitance (C_{Buck})	4740	µF
Output capacitance (C_{out})	5924.48	µF
Output voltage for bus (V_{out})	48	V

5.3 *MPPT charge control*

Environmental factors such as shading, cloudiness, dust, snow accumulation, solar irradiance, ambient temperature, and operational conditions such as varying load impedance, battery charging conditions, and PV system configuration

(string vs array) directly influence the power that can be extracted from the solar PV array relative to the voltage across its output. A maximum power point charge controller is deployed to dynamically adjust the system's operating point on the P-V curve in order to extract maximum power from the solar PV source, required to drive the sucker rod pump and charge the battery. The MPPT algorithm varies the duty cycle of the DC-DC buck converter hence changing the effective impedance of the load across the buck converter. This adjusts the voltage of the solar PV source and ultimately controls the output power the array delivers. The Perturb and Observe (P&O) method operates by making small, deliberate adjustments to the PV array's operating voltage and monitoring the resulting power output changes. The controller systematically modifies the voltage in discrete steps, analyzing how each change affects the array's power production as seen in Figure 28.

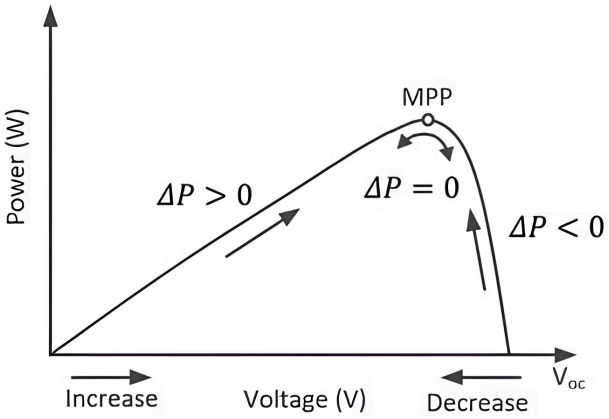

Figure 28. MPPT controller using perturb and observe (P&O) algorithm

This iterative process is shown in Figure 29 and continues, with the system adjusting the voltage either upward or downward, until it identifies the optimal operating point where maximum power extraction occurs.

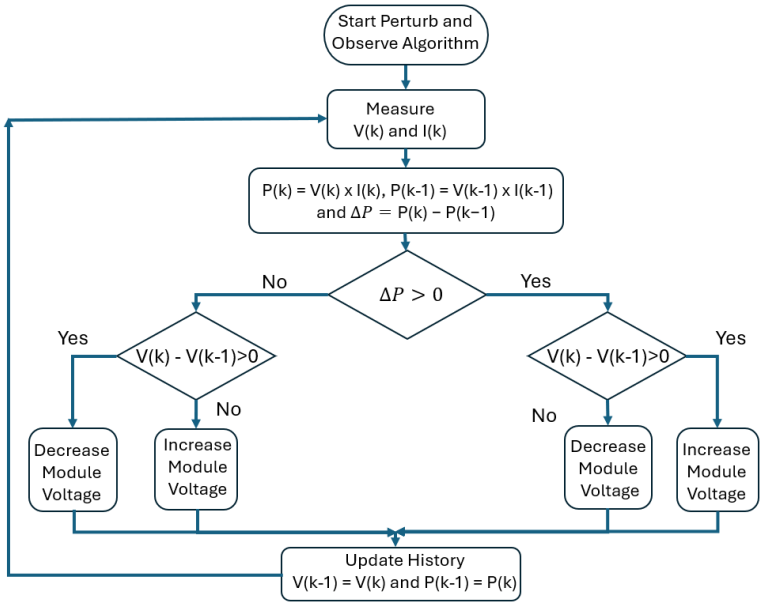

Figure 29. Flow chart and representation of perturb and observe (P&O) algorithm for MPPT

The algorithm deployed in Simscape maintains this exploration pattern, constantly fine-tuning the operating point to ensure the PV array delivers its peak performance despite varying environmental conditions. The representation of the P&O algorithm for MPPT in Simscape is shown in Figure 30.

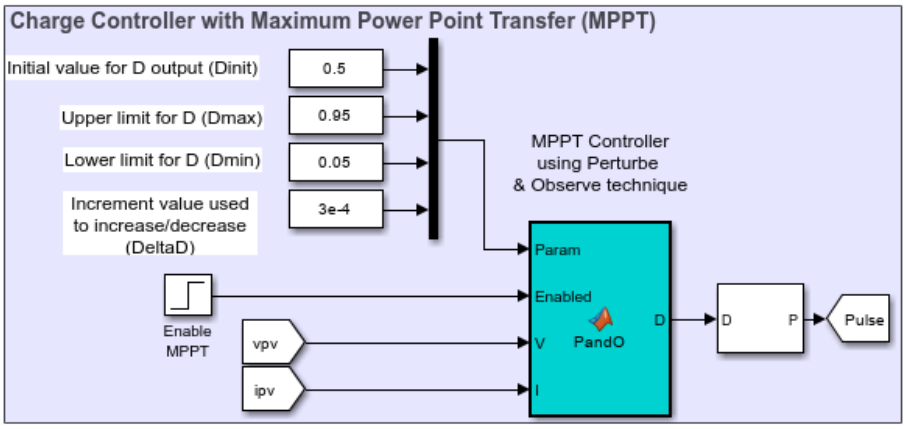

Figure 30. Perturb and observe algorithm with MPPT strategy in simscape

5.4 *Battery energy storage system (BESS)*

The battery energy storage system consists of a total of 64 lead-acid batteries, made up of 4 batteries per string, grouped as 16 strings of lead-acid batteries, and the DC-DC buck converter serves as the battery charge controller. The battery stores excess electricity during periods of high PV power output and augments the system, when there is a shortfall in generated power due to adverse environmental and operating conditions. Given the capacity per battery is 219 Ah, the rated capacity for 16 strings is 219 *16 = 3504 Ah.

The total amount of energy that the battery bank can store and release under optimal conditions is given by the nominal capacity, and for 64, 12 V batteries of 219 Ah current capacity, the nominal capacity is 64*12*219 = 168, 192 VAh or 16.192 kWh. The rated current capacity is nominal capacity divided by bus voltage (16.192 kWh/48 V) = 3504 Ah. The parameters for the design and sizing of the battery energy storage system (BESS) are given in Table 6 and Figure 31. The equivalent circuit for modelling the BESS is presented in Figure 32.

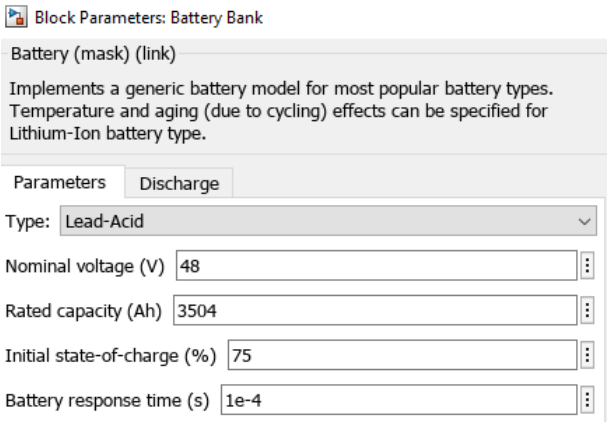

Figure 31. Design specifications of BESS

Table 6. BESS parameters

Battery bank data	Ratings	Unit
Number	64	(4 bt/string)
Strings in parallel	16	Strings
Bus voltage	48	V
Nominal capacity	168	kWh
Usable nominal capacity	118	kWh
Energy in	3860	kWh/yr
Energy Out	3294	kWh/yr

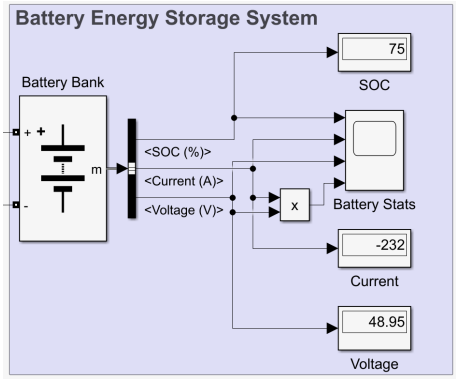

Figure 32. Equivalent circuit of battery energy storage system

5.5 *Power conditioning system*

The power conditioning system consists of a 3-phase inverter for converting the DC from the solar PV source to alternating current in the charging cycle during the day, and for converting stored DC battery power into AC during the discharging cycle at low irradiance. A three-phase two-winding transformer also transforms the low voltage, high current inverter output, into a high voltage, low current output, suitable for the three-phase squirrel cage induction motor. To relate the DC bus voltage to the AC line-to-line voltage output, we use the formula:

$$m \times \frac{V_{DC}}{\sqrt{2}} = V_{L-L(rms)} \tag{4}$$

The step-up transformer has a voltage transformation ratio ($\frac{V_1}{V_2}$) of 30/460 and the line-to-line rms voltage, hence the RMS inverter output voltage $V_{L-L(rms)} = m \times 0.7071 \times V_{DC}$, assuming modulation index is m = 1.0. The inverter system has a bus input voltage of ~48 V,

$$V_{L-L(rms)} = 0.7071 * 48 = 33.84\ V.$$

To supply the power required by the electric motor, a step-up transformer of 7 kVA, and a primary to secondary voltage ratio of 30/460 at 60 Hz are selected and deployed. The equivalent circuit for modelling the power conditioning system is presented in Figure 33a. The parameters for the design and sizing of the power conditioning system are given in Table 7 and Figure 33b.

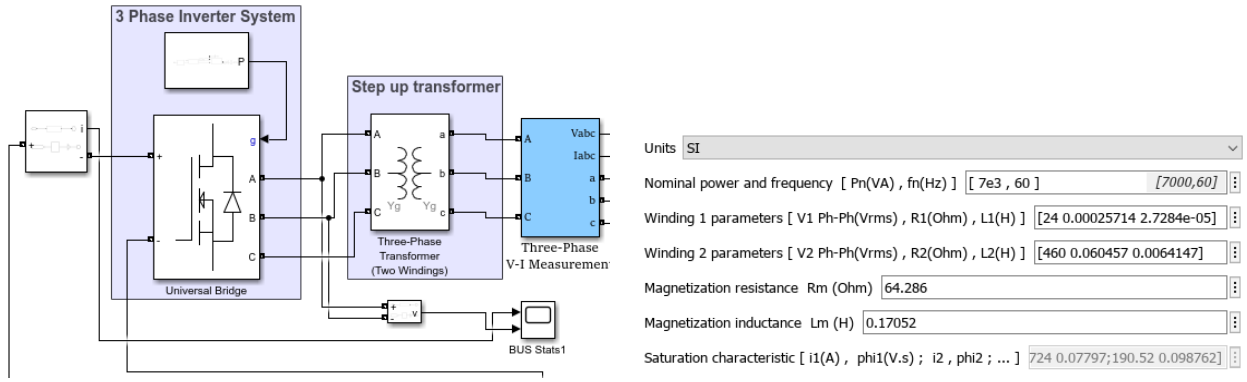

(a) (b)

Figure 33. An equivalent circuit of a power conditioning system for the induction motor load. (**a**) Equivalent circuit of a power conditioning system. (**b**) Design parameters

Table 7. Power conditioning system parameters

Power conditioning system parameters	Ratings	Unit
Primary voltage (V_1)	30	V
Secondary voltage (V_2)	460	V
Frequency (f)	60	Hz
RMS line-to-line voltage $V_{L-L(rms)}$	33.84	V
Nominal power	7	kVA
Modulation index, m (assumed)	1	

5.6 *Mechanical waveform input*

The mechanical torque profile of the induction motor is defined by the sinusoidal waveform shown in Figure 34. It defines the parameters for the pump torque profile as per unit. The pump operates in a cyclic motion to lift oil from the subsurface. The torque requirement of the motor fundamentally varies throughout each stroke cycle due to the higher torque needed to lift the fluid column in the upstroke and the lower torque required in the down stroke as gravity assists the motion. The mechanical torque function block T_m simulates the mechanical input torque for the balanced operation of the motor, accounting for the impact of the counterbalance weights in the up-stroke, hence the waveform is symmetrical.

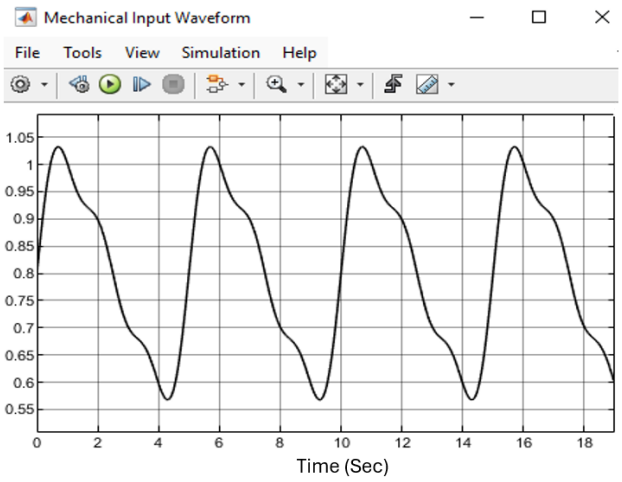

Figure 34. The waveform of mechanical torque requirement of Squirrel cage induction motor

5.7 *Load system*

The electrical motor system is a three-phase squirrel cage induction motor that operates at a line-to-line voltage of 460 volts receiving power from the solar PV system and driving the mechanical load of the sucker rod pump. The theoretical peak load is 4.44 kW. Considering the output mechanical power of the squirrel cage induction motor type AEEAFP (067R50) from [39] rated 7.5 hp, 1110 full load rpm, at a frequency of 60 Hz, with power factor of 0.83 and full load current and efficiency of 10 A and 83.5% respectively. The full load torque is 35.4 lb-ft at nominal power P_n (kVA) rating is (7.5*0.7457)/(0.83) = 6.74 kVA, with a safety factor (SF) of 1.15. Number of poles p = 120*f/N_s = (120*60)/1200 = 6 poles (3 pole pairs). The parameters for the sizing of the 3-phase squirrel cage induction motor are given in Table 8.

Table 8. Showing name plate 3 phase induction motor parameters

Motor parameters	Ratings	Unit
Line-to-line voltage	460	V
Full load current	10	A
Peak load	4.44	kW
Rated power	7.5	hp
Full load speed	1110	rpm
Full load torque	35.4	lb-ft
Efficiency	83.5	%
Power factor	0.835	
Safety factor	1.15	

The peak power available to the squirrel cage induction motor load = 0.835 (7.5*0.7457) = 4.67 kW, which is sufficient to drive the sucker rod pump load of peak load 4.44 kW. The equivalent circuit of the electric motor load system is presented in Figure 35.

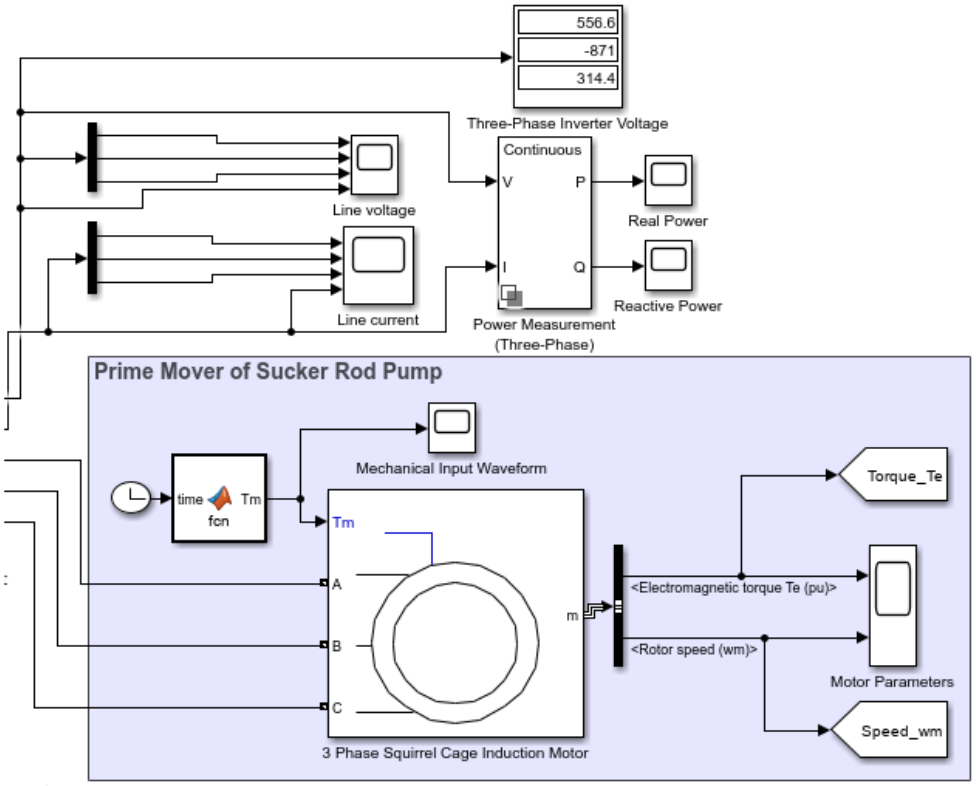

Figure 35. Equivalent circuit of the squirrel cage Induction motor prime mover

6. Analysis of results

The simulation examines system performance under changing environmental conditions. The impact of solar irradiance in W/m^2 and the ambient temperature in degrees Celsius are simulated. The location of interest is an idle well in the town of Medicine Hat in Alberta, Canada as presented in a previous work by the authors [32]. As expected in the northern hemisphere, the average hourly solar irradiance, average hourly temperature and the length of daytime solar exposure is generally higher in summer than in winter. Using June as a sample summer month in Medicine Hat, it is shown to have longer daytime hours and higher levels of solar irradiance, with warmer temperatures. In comparison with January taken as a sample winter month which is observed to have shorter hours and lower levels of solar irradiance, at lower temperatures. The impact of weather and environmental fluctuations on the system's effectiveness is carefully studied and presented in Figures 36–40. Key measured parameters reveal that overall system performance remains robust and satisfactory during steady-state operation, with momentary deviations staying within design parameters.

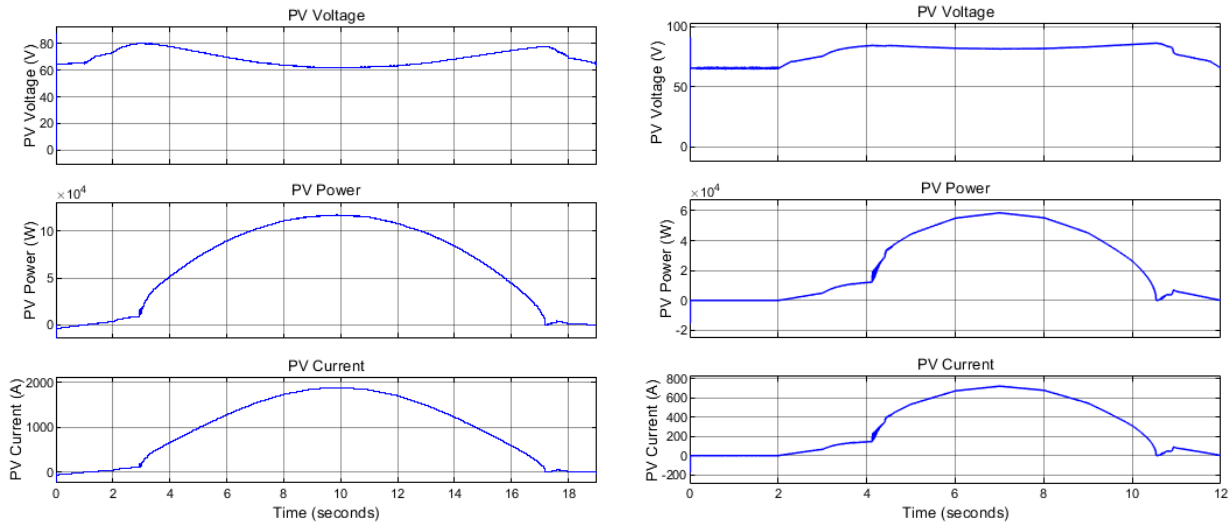

Figure 36. Solar PV voltage, current, and power. (**a**) Summer. (**b**) Winter

The maximum power point tracking system implemented with the solar PV source continuously monitors the incremental changes in the power generated and compares with the incremental voltage changes, ensuring that the maximum power is being received by the electric motor and the excess power generated is provided to charge the battery energy storage system. This is achieved by effectively matching of the source to load impedance and facilitating maximum transfer of power from the solar PV source to the load. As environmental parameters shift, the tracker identifies new optimal operating points, supplying the power needed to provide the needed motor torque and maintain optimal performance despite the fluctuating power availability from the solar PV array. This ensures that sufficient charging current is delivered to the energy storage system to maintain the bus voltage. As shown in the state of charge from Figure 37, at low solar irradiance, the battery supplies the energy required to sustain production and drains, while during the day, it charges, while the load receives the energy required to sustain production.

From Figure 37, the current, voltage and power of the battery energy storage system are steady, predictable and consistent with the expected behavior for steady state operation. Considering state of charge, in summer it increases gradually from ~75% to ~90% over 19 s, while winter shows similar upward trend from ~75% to ~85% over 12 s. Considering current and voltage stability, both seasons show relatively stable current oscillating around $\pm 2 \times 10^5$ A, voltage remains consistent around 60–80 V in both cases. Winter profile shows slightly less fluctuation in both parameters. The power fluctuates between approximately -2×10^7 to 2×10^7 W. The plot shows similar power profiles between seasons

though winter shows marginally less variation, both maintain consistent power delivery despite seasonal differences. Although summer profile runs longer (19 s vs 12 s), winter shows slightly more stable parameters with less fluctuation, winter also achieves lower maximum SOC (~85% vs ~90%) and demonstrates marginally better parameter stability overall. This comparison suggests the battery system maintains reliable performance across seasonal variations, with winter operation showing slightly more stable characteristics despite shorter operating duration.

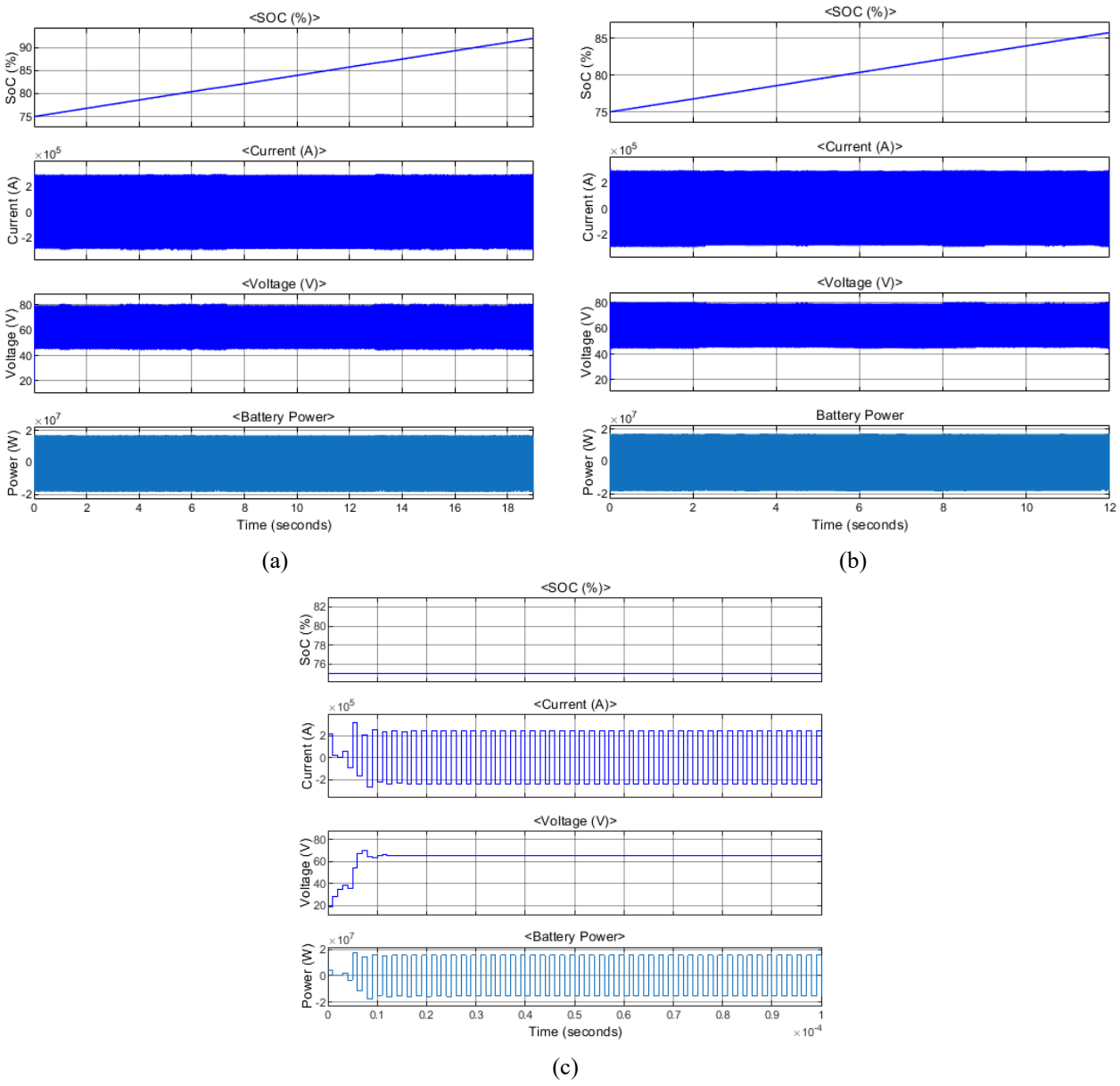

Figure 37. Battery state of charge (SOC%), current, voltage, and power for battery energy storage system. (**a**) Summer. (**b**) Winter. (**c**) Battery parameters (higher resolution)

The pulsating direct current (DC) power supply (from the solar PV system and the battery backup) is converted to alternating current (AC) by the three-phase inverter system and the sinusoidal line voltages and line currents received by the three-phase squirrel cage induction motor are given in Figure 38a,b, respectively.

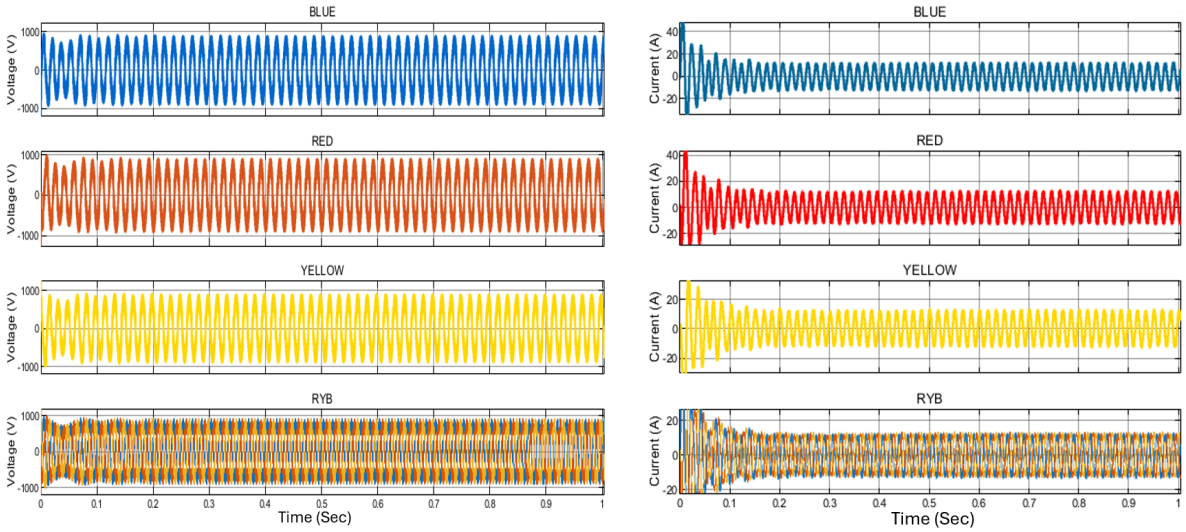

Figure 38. Similar sinusoidal load current and voltage I_{RYB}, V_{RYB} for summer and winter. (**a**) Sinusoidal load voltage V_{RYB}. (**b**) Sinusoidal load current I_{RYB}

The active and reactive power of the induction motor in summer and winter is presented in Figures 39 and 40. The load is observed to have significant reactive power demand. Comparing Figures 39a and 40a, summer is observed to have more pronounced variations in its real power demand compared to winter and comparing Figures 39b and 40b, summer also shows periodic sharp transitions in the reactive power demand.

Per unit torque and speed characteristics of the 3-phase squirrel cage induction motor are given in Figure 41. The system reaches a relatively stable operating point after the initial transient period. The persistent torque oscillations indicate mechanical system dynamics due to the sucker rod load fluctuations.

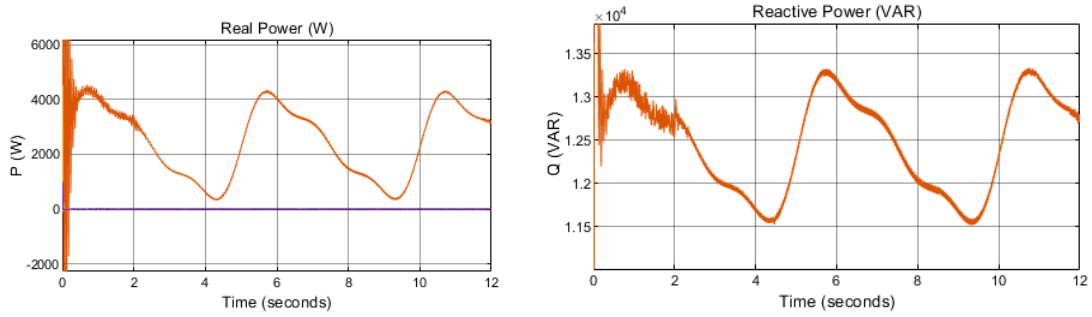

Figure 39. Similar real and reactive power demand for winter. (**a**) Real power demand. (**b**) Reactive power demand

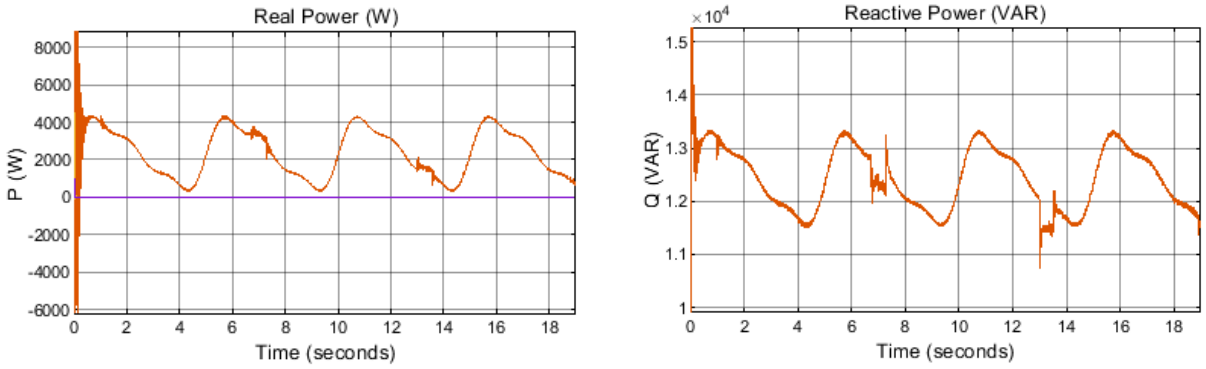

(a) (b)

Figure 40. Similar real and reactive power demand for summer. (**a**) Real power demand. (**b**) Reactive power demand

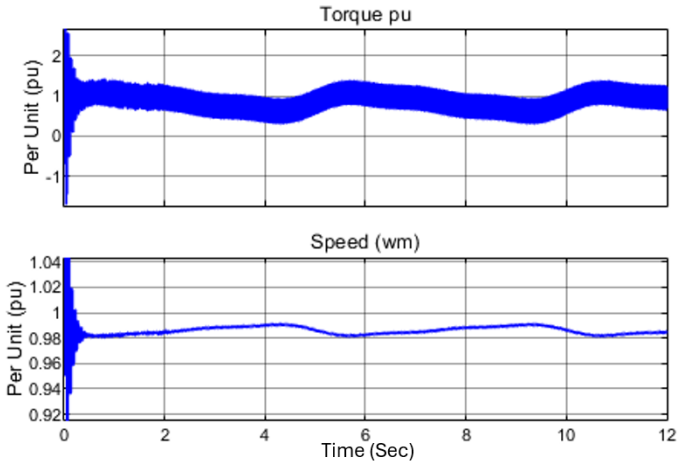

Figure 41. Similar torque and speed characteristics for summer and winter

From the analysis of incorporating the representative solar irradiance and temperature data for the location, the design ensures that the required load current and voltage are sustained, irrespective of environmental fluctuations, and the real power from the solar PV array and battery storage is demonstrated to be sufficient to drive the load and charge the battery. It can be inferred that the lower power output anticipated due to reduced irradiance levels for winter is compensated for by the improved semiconductor efficiency at cold temperatures. Correspondingly, higher energy generation due to increased irradiance and longer days in summer are counterbalanced by temperature-induced efficiency losses during peak heat periods.

The results of the simulations indicate that the Simscape/Simulink model provides a detailed representation of sucker rod pump dynamics. Simulating mechanical and electrical microgrids within a single framework, this offers significant advantages for understanding and optimizing pump performance. The integration of summer and winter irradiance and temperature data in the analysis provides a clear indication of the system's performance under various environmental and operational conditions. The MPPT battery charge control strategies further enhances the model's capability to optimize performance under varying load conditions, while the energy storage system ensures the load demands can still be met at lower irradiance levels and durations. The integrated model of the solar powered sucker rod pump is presented in Figure 42, showing the various subsystems modeled in this research work. The comprehensive system model for an oil well pumping system, integrates electrical, mechanical, and hydraulic components in a single unified design. The schematic diagram emphasizes the power transmission path from electrical input through mechanical systems to the final pumping action.

Although the subsurface pump and downhole tubing subsystem are included in the schematic, analysis and visualization of the metrics in this subsystem is beyond the scope of this research.

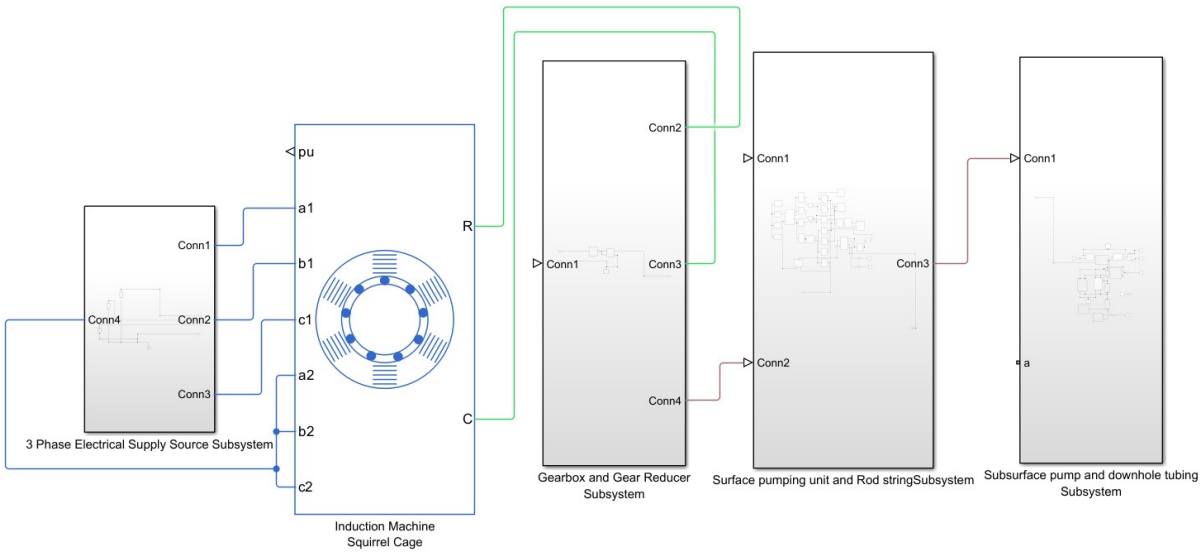

Figure 42. Schematic diagram of integrated sub-systems in model-based simulation

7. Conclusions

The integrated design, modelling, simulation, and control of a solar-powered sucker rod oil well within a single simulation environment offers significant advantages for understanding and optimizing sucker rod pump systems. This comprehensive study focuses on developing an integrated model for solar-powered sucker rod pumps, integrating both mechanical and electrical subsystems to optimize overall performance. The research employs a systematic approach by decoupling the microgrid into distinct subsystems, enabling detailed analysis and efficiency improvements from the solar PV source through to the electric motor load. The methodology combines modelling tools including SolidWorks for mechanical design and Simscape for electrical characteristics, creating a digitally representative model that facilitates system optimization before physical implementation. The integration of energy storage solutions and control systems, coupled with extensive simulation testing under various scenarios, demonstrated reliable operation despite ambient temperature variation and solar intermittency, while providing a robust framework for performance evaluation and system refinement. Key performance indicators such as solar PV power, battery power, bus voltage, step-up transformer rating, and real and reactive power requirements of the sucker rod pump system are visualized in the model. The files and intellectual property created in executing this research are shared by the author and available from [40].

8. Organization of the work

This work is a comprehensive study of the design, dynamic modelling, simulation and control of a sucker rod oil pump and its integration with a solar power system. The content is organized into several main sections and subsections. The chapter begins with an introduction and objectives, followed by a system description. The methodology forms the core of the work, divided into four main parts: modelling the sucker rod pump in SolidWorks and Simscape, detailed analysis of model-based subsystems, methodology for modelling a solar-powered sucker rod oil pump, and PV system design. Each of these sections is further broken down into specific components and processes, such as the prime mover, gearbox, surface pumping unit, and subsurface pump for the sucker rod system, and various elements of the solar power

system including the PV array, DC-DC converter, MPPT charge control, and battery storage. The research concludes with an analysis of the simulation outcome, providing a logical flow from conceptualization and modelling to results analysis.

Conflict of interest

The authors declare no conflict of interest.

References

[1] M. Kang, A. R. Brandt, Z. Zheng, J. Boutot, C. Yung, A. S. Peltz, et al., "Orphaned oil and gas well stimulus—Maximizing economic and environmental benefits," *Elem. Sci. Anth.*, vol. 9, no. 1, p. 00161, 2021.

[2] K. El Hachem and M. Kang, "Reducing oil and gas well leakage: a review of leakage drivers, methane detection and repair options," *Environ. Res.: Infrastruct. Sustain.*, vol. 3, no. 1, p. 012002, 2023.

[3] N. Anglani, S. R. Di Salvo, G. Oriti, and A. L. Julian, "Renewable energy sources and storage integration in offshore microgrids," in *Proc. 2020 IEEE Int. Conf. Environ. Electr. Eng. 2020 IEEE Ind. Commer. Power Syst. Europe*, Madrid, Spain, Jun. 9–12, 2020.

[4] D. Raimi, A. J. Krupnick, J. S. Shah, and A. Thompson, "Decommissioning orphaned and abandoned oil and gas wells: New estimates and cost drivers," *Environ. Sci. Technol.*, vol. 55, no. 15, pp. 10224–10230, 2021.

[5] G. Takacs, *Sucker-rod Pumping Handbook: Production Engineering Fundamentals and Long-Stroke Rod Pumping*. Houston, TX, USA: Gulf Professional Publishing, 2015.

[6] S. Fakher, A. Khlaifat, M. E. Hossain, and H. Nameer, "A comprehensive review of sucker rod pumps' components, diagnostics, mathematical models, and common failures and mitigations," *J. Pet. Explor. Prod. Technol.*, vol. 11, no. 10, pp. 3815–3839, 2021.

[7] Alberta Energy Regulator (AER), "Methane Reduction," Accessed: Nov. 27, 2024. https://www.aer.ca/protecting-what-matters/protecting-the-environment/methane-reduction.

[8] Alberta Energy Regulator (AER), "Well Status," Accessed: Nov. 27, 2024. https://www.aer.ca/providing-information/data-and-reports/data-hub/well-status.

[9] D. Schiffner, M. Kecinski, and S. Mohapatra, "An updated look at petroleum well leaks, ineffective policies and the social cost of methane in Canada's largest oil-producing province," *Clim. Change*, vol. 164, no. 3, p. 60, 2021.

[10] Office of the Parliamentary Budget Officer, "Estimated Cost of Cleaning Canada's Orphan Oil and Gas Wells," 2022. Accessed: Nov. 27, 2024. https://www.pbo-dpb.ca/en/publications/RP-2122-026-S-estimated-cost-cleaning-canada-orphan-oil-gas-wells-cout-estimatif-nettoyage-puits-petrole-gaz-orphelins-canada.

[11] C. Temizel, H. Aydin, F. B. Hosgor, C. Yegin, and C. S. Kabir, "Green Energy Sources Reduce Carbon Footprint of Oil & Gas Industry Processes: A Review," *J. Energy Power Technol.*, vol. 5, no. 1, pp. 1–25, 2023.

[12] A. Yashin, A. Konev, and M. Khakimyanov, "Power Supply of The Sucker Rod Pump Unit Electric Drive Using Renewable Energy Sources," in *Proc. 2021 Int. Conf. ElectroTech. Comp. Syst.*, Ufa, Russian Federation, Nov. 16–18, 2021, pp. 43–46.

[13] M. Elyamany, S. O. Abdellatif, and H. Ghali, "Online Sucker-Rod Pumping With Photovoltaic Driven System Sizing Tool for Oil and Gas Industrial Sector," in *International Conference on Remote Engineering and Virtual Instrumentation*. Cham, Switzerland: Springer International Publishing, Feb. 2022, pp. 174–185.

[14] C. A. Osaretin, S. D. Butt, and M. T. Iqbal, "Sizing, Parametric Investigation and Analysis of Automated Sucker Rod Pump using Beam Pump Simulators," *Eur. J. Electr. Eng. Comput. Sci.*, vol. 4, no. 5, p. 16227, 2020.

[15] SolidWorks, "Simscape Multibody Link," Accessed: Aug. 15, 2024. https://www.solidworks.com/partnerproduct/simscape-multibody-link.

[16] MathWorks, "Export a SolidWorks Robot Assembly Model—MATLAB & Simulink," Accessed: Aug. 15, 2024. https://www.mathworks.com/help/smlink/ug/export-robot-assembly-from-solidworks-software.html.

[17] MathWorks, "Import SolidWorks Assemblies into Simscape Multibody," Accessed: Aug. 15, 2024. https://www.mathworks.com/videos/import-solidworks-assemblies-into-simscape-multibody-1701670328083.html.

[18] MathWorks, "SolidWorks—MATLAB & Simulink," Accessed: Aug. 15, 2024. https://www.mathworks.com/help/smlink/solidworks.html.

[19] MathWorks, "CAD Translation [Online]," Accessed: Aug. 14, 2024. https://www.mathworks.com/help/physmod/sm/ug/cad-translation.html.
[20] E. Mishchenko and V. Mishchenko, "Exploring the cad model of the manipulator using cad translation and simscape multibody," *E3S Web Conf.*, vol. 279, p. 03014, 2021.
[21] G. Boschetti and T. Sinico, "Designing Digital Twins of Robots Using Simscape Multibody," *Robotics*, vol. 13, no. 4, p. 62, 2024.
[22] S. Tickoo, *Learning SOLIDWORKS 2019: A Project Based Approach*. Pendleton, IN, USA: CADCIM Technologies, 2019.
[23] MathWorks, n.d. "Modeling Joint Connections—MATLAB & Simulink," Accessed: Aug. 14, 2024. https://www.mathworks.com/help/physmod/sm/ug/modeling-joint-connections.html.
[24] MathWorks, n.d. "Mates and Joints—MATLAB & Simulink," Accessed: Aug. 14, 2024. https://www.mathworks.com/help/smlink/ref/mates-and-joints.html.
[25] MathWorks, n.d. "Constraints and Joints—MATLAB & Simulink," Accessed: Aug. 14, 2024. https://www.mathworks.com/help/sm/ug/constraints-and-joints.html.
[26] U. Corrales, "A simple example of beam pump mechanism in SolidWorks," Accessed: Apr. 14, 2024. https://grabcad.com/library/beam-pump-3.
[27] C. A. Osaretin, T. Iqbal, and S. Butt, "Optimal sizing and techno-economic analysis of a renewable power system for a remote oil well," *AIMS Electron. Electri. Eng.*, vol. 4, no. 2, pp. 132–153, 2020.
[28] A. V. Semenov, S. I. Tecle, and A. Ziuzev, "Modeling induction motor driven sucker rod pump in MATLAB Simscape," in *Proc. 2020 Russ. Workshop Power Eng. Autom. Metall. Ind. Res. Pract.*, Magnitogorsk, Russia, Sept. 25–26, 2020, pp. 67–71.
[29] SMLease Design, "Gear Train: Gear Ratio, Torque and Speed Calculations," Accessed: Nov. 28, 2024. https://smlease.com/entries/mechanism/gear-train-gear-ratio-torque-and-speed-calculation/.
[30] The MathWorks Inc., "Rotational Multibody Interface Documentation," Accessed: Nov. 27, 2024. https://www.mathworks.com/help/simscape/ref/rotationalmultibodyinterface.html.
[31] The MathWorks Inc., "Gear Box Documentation," Accessed: Nov. 27, 2024. https://www.mathworks.com/help/simscape/ref/gearbox.html.
[32] L. Lao and A. Leuterman, "Torsional Vibration of Sucker Rod Strings," in *SPE Annual Technical Conference and Exhibition*, Houston, TX, USA: Society of Petroleum Engineers, 2012, SPE-159703-MS.
[33] The MathWorks Inc., "Translational Multibody Interface Documentation," Accessed: Nov. 27, 2024. https://www.mathworks.com/help/simscape/ref/translationalmultibodyinterface.html.
[34] Environment and Climate Change Canada, "Engineering Climate Datasets," Accessed: Nov. 28, 2024. http://climate.weather.gc.ca/prods_servs/engineering_e.html.
[35] Government of Canada, "Historical Climate Data: Hourly Data Report for January 31, 2017—Climate—Environment and Climate Change Canada," Accessed: Nov. 28, 2024. https://climate.weather.gc.ca/prods_servs/engineering_e.html.
[36] Government of Canada, "Historical Climate Data: Hourly Data Report for June 1, 2017—Climate—Environment and Climate Change Canada," Accessed: Nov. 28, 2024. https://climate.weather.gc.ca/prods_servs/engineering_e.html.
[37] B. Singh, U. Sharma, and S. Kumar, "Standalone photovoltaic water pumping system using induction motor drive with reduced sensors," *IEEE Trans. Ind. Appl.*, vol. 54, no. 4, pp. 3645–3655, 2018.
[38] Texas Instruments, "BUCK-CONVCALC: Component Calculator for BUCK Converters," Accessed: Nov. 28, 2024. https://www.ti.com/tool/BUCK-CONVCALC.
[39] TECO-Westinghouse Motors (Canada) Inc., "NEMA Premium Efficiency ODP—Commercial Duty," Accessed: Nov. 28, 2024. https://tecowestinghouse.ca/motors/low-voltage/optim-odp/.
[40] C. A. Osaretin, n.d. "Sucker Rod Pump Modeling," Accessed: Dec. 30, 2024. https://github.com/caosaretin/Sucker-Rod-Pump-Modeling.